

Orthogonal Chirp-Frequency Division Multiplexing

Túlio Fernandes Moreira¹, Mateus de Lima Filomeno², Wallace Alves Martins³, *Senior Member, IEEE*,
and Moisés Vidal Ribeiro⁴, *Senior Member, IEEE*

Abstract—This paper introduces a multicarrier communication technique termed orthogonal chirp-frequency division multiplexing (OCFDM). It relies on a unitary transform named discrete modular chirp transform. The proposed OCFDM amalgamates characteristics from the orthogonal frequency division multiplexing (OFDM) and orthogonal chirp division multiplexing (OCDM), partitioning the frequency spectrum into distinct subbands and populating each of them with orthogonal chirps. By deriving the reconstructed signal at the receiver, the paper shows that the normalized signal-to-noise ratio exhibits changes across subbands, allowing the use of resource allocation, for instance, for power allocation or bit-loading. Moreover, it is shown that the OCFDM introduces an additional degree of freedom through its tile geometries, allowing it to be configured to perform in between OFDM and OCDM and, consequently, to offer novel and balanced trade-offs among symbol error rate, data rate, and robustness to interference. Numerical analyses illustrate those trade-offs and confirm the versatility and efficacy of the OCFDM.

Index Terms—Chirp spread spectrum, frequency division, multicarrier communication, resource allocation.

I. INTRODUCTION

THE widespread use of orthogonal frequency division multiplexing (OFDM) has long shaped the data communication domain. From its use as a key component in 4G Long-Term Evolution (LTE) networks around 2010 to its wide adoption in various technologies, including Wi-Fi, power line communication (PLC), and digital television, OFDM has been instrumental in efficiently utilizing the available frequency band [1]. However, as communication technologies advance and demands evolve, researchers have explored alternative

multiplexing techniques to enhance performance and address new challenges. In this context, the orthogonal chirp division multiplexing (OCDM) technique has been assessed in various scenarios [2], [3], [4], [5], showcasing its potential superiority over OFDM under some constraints.

The OCDM is a chirp spread spectrum (CSS)-based multicarrier data communication technique especially attractive because of both its enhanced symbol error rate (SER) performance, when compared to the OFDM, and its robustness against various impairments in single-input single-output (SISO) [6] and multiple-input multiple-output (MIMO) [7] communication systems. The authors in [8] showed how the OCDM takes advantage of the discrete Fresnel transform (DFnT) to create chirped waveforms that are orthogonal among each other and robust to carrier frequency offset (CFO), narrowband interference, and time-burst interference. Furthermore, the chirp waveform characteristics of the OCDM also benefit channel characterization, synchronization, and sensing properties of communication. For instance, the work in [9] shows that the OCDM can characterize the whole frequency band using only one chirp; the work in [10] discusses a pilot signal for high-precision characterization of channels; the work in [11] presents a pilot signal for joint characterization and synchronization. Regarding sensing capabilities, the works in [12], [13], and [14] describe the use of OCDM in joint radar-communication scenarios and compare it with other techniques; a similar study is reported in [15] for PLC scenarios. Also, the authors in [16], [17], and [5] analyzed the OCDM performance in underwater acoustic communication. In contrast, the authors in [4] proposed the hybrid PLC/wireless system based on OCDM.

While the OCDM has some appealing features as a chirp-based multicarrier data communication technique, there are still opportunities for further enhancements, and novel works have been developed to this end. The affine frequency division multiplexing (AFDM) is a recent CSS-based technique that uses the discrete affine Fourier transform (DAFT), a general transform expression from which the discrete Fourier transform (DFT) and DFnT can be derived [18]. This technique excels in linear time-varying (LTV) channels by tuning the DAFT parameters to match the channel's maximum delay and normalized Doppler shift. DAFT attains a similar bit-error rate (BER) performance to the orthogonal time frequency space (OTFS) system [19], another multicarrier system quite investigated for LTV scenarios.

Received 20 February 2024; revised 10 July 2024 and 23 October 2024; accepted 28 November 2024. Date of publication 5 December 2024; date of current version 17 July 2025. This research was supported in part by Coordenação de Aperfeiçoamento de Pessoal de Nível Superior (CAPES) under Grant 001, Conselho Nacional de Desenvolvimento Científico e Tecnológico (CNPq) under grants 404068/2020 and 314741/2020-8, Fundação de Amparo à Pesquisa do Estado de Minas Gerais (FAPEMIG) under grants APQ-03609-17 and APQ-04623-22, and Instituto Nacional de Energia Elétrica (INERGE). An earlier version of this paper was presented at the 2023 Symposium on Internet of Things (SIoT) [DOI: 10.1109/SIoT60039.2023.10390373]. The associate editor coordinating the review of this article and approving it for publication was O. Günlü. (Corresponding author: Túlio Fernandes Moreira.)

Túlio Fernandes Moreira, Mateus de Lima Filomeno, and Moisés Vidal Ribeiro are with the Department of Electrical Engineering, Federal University of Juiz de Fora, Juiz de Fora 36036-900, Brazil (e-mail: tuliofmoreira3@gmail.com; delimafilomeno@gmail.com; moises.ribeiro@ufjf.br).

Wallace Alves Martins is with the Fédération ENAC ISAE-SUPAERO ONERA, Université de Toulouse, 31055 Toulouse, France (e-mail: wallace.martins@isae-supaero.fr).

Digital Object Identifier 10.1109/TCOMM.2024.3511715

In frequency selective linear time invariant (LTI) channels, which is this paper's focus, the performance of the AFDM and OCDM techniques are equivalent [18]. Also, the OCDM possesses a low average signal-to-noise ratio (SNR) compared to other systems such as the OFDM and orthogonal time-frequency division multiplexing (OTFDM), resulting in a lower data rate [20]. Moreover, the inflexibility of an OCDM transmission frame, where each chirp occupies the entire frequency band and symbol period, makes it challenging to implement resource allocation [21] seamlessly. To enable resource allocation in OCDM techniques, similar to the OFDM technique, preprocessing steps that modify the transmitted signal characteristics are required, as pointed out in [22]. To our knowledge, no studies on resource allocation for CSS-based multicarrier techniques parallel what was done in OFDM. This gap likely stems from their channel-to-noise gains, which are constant across its chirps due to their symbol spreading through the whole frequency band.

To address these critical issues, we propose a novel transform, called discrete modular chirp transform (DMCT), capable of creating divisions in the available frequency band, named voices, and filling them with orthogonal chirps. This transform can be interpreted as the combination of the discrete orthonormal S-transform (DOST) [23], [24], which creates a modular tile geometry in the time-frequency plane, and the DFNT, which defines the orthogonal chirps within each voice. Relying on the DMCT, we propose the orthogonal chirp-frequency division multiplexing (OCFDM) technique to ensure that the chirped waveforms of transmitted signals are confined to distinct portions of the frequency band. Moreover, the OCFDM can be interpreted as a hybrid technique grounded on OFDM and OCDM, hence benefiting from the data communication characteristics of both of them, *i.e.*, the CSS and the frequency division features. The CSS feature provides robustness against interference, a property that the OFDM does not possess. On the other hand, the frequency division creates voices with different SNRs, thus enabling resource allocation and increasing the data rate of CSS-based techniques, which is not possible in OCDM. An initial and brief discussion of this investigation was presented in [25].

A. Main Contributions and Findings

In summary, the main contributions of this work are:

- The introduction of a novel discrete transform, namely DMCT. This unitary transform is based on the DOST and DFNT and can create a flexible division within the available frequency band.
- The proposal of a novel data communication technique, namely OCFDM. This technique uses the DMCT in its core, taking advantage of frequency division and chirp-waveform features to be a CSS-based data communication technique with flexible characteristics.
- The introduction of resource allocation capability, based on frequency division, in CSS-based multicarrier techniques. This feature makes the OCFDM achieve a higher data rate than the OCDM while preserving crucial features like robustness to interference.

A numerical performance assessment of the OFDM, OCDM, and the proposed OCFDM is reported, considering different tile geometries for the proposed OCFDM. Our major findings are:

- The arrangement of voices in the OCFDM technique is influenced by the chosen tile geometry, and it directly impacts the SNR experienced by each chirp. This additional degree of freedom of selecting the tile geometry results in a trade-off between SER, data rate, and robustness against interference.
- Regarding the uncoded SER, the proposed OCFDM outperforms the traditional OFDM. Notably, OCFDM preserves the robustness to interference inherent in CSS-based techniques and maintains commendable SER even in the presence of interference due to cyclic prefix (CP) length violation, symbol timing offset (STO), and CFO, albeit not outperforming the OCDM.
- Simulations of coded BER shows that the OCFDM performs better than the OFDM with convolutional codes with high code rate and similar to it with low-density parity-check (LDPC) codes.
- In terms of data rate, the OCFDM outperforms the OCDM, performing closer to the OFDM's data rate for all geometries considered in this paper. Also, the OCFDM presents a far lower feedback complexity for resource allocation algorithms.
- When compared to the OTFDM, the OCFDM presents the same advantages of less channel state information (CSI) feedback, SER, and data rate. However, the OCFDM attains superior robustness against interference.

Overall, the flexibility offered by the OCFDM enables distinct trade-offs in performance and robustness compared to those provided by the OFDM and OCDM.

B. Organization

The remainder of this paper is organized as follows: Section II details the DOST and the coordination parameters, laying the ground for Section III wherein we present the DMCT, its unitary property, and some prebuilt geometries. Section IV describes the OCFDM technique and details the mathematical derivation of the reconstructed signal, SNR, and normalized signal-to-noise ratio (nSNR). Section V focuses on the performance comparisons among the proposed OCFDM and other techniques from the literature. Last, Section VI outlines our concluding remarks.

C. Notation

In this article, $\mathbb{E}\{\cdot\}$ denotes the expectation operator, whereas $(\cdot)^T$, $(\cdot)^*$, and $(\cdot)^\dagger$ denote the transpose, conjugate, and conjugate transpose operators, respectively. Moreover, $\mathbf{0}_{a \times b}$ stands for an $(a \times b)$ -size matrix of zeros and \mathbf{I}_c is an c -size identity matrix. $\mathbf{F}_N \in \mathbb{C}^{N \times N}$ is the N -size normalized DFT matrix such that its $(k, n)^{\text{th}}$ element is equal to $F_{N,k,n} = \exp(-j2\pi kn/N)/\sqrt{N}$ with $N = 2^d$ for $d \in \mathbb{N}^*$. Also, Φ_N is the N -size normalized DFNT matrix with the $(m, n)^{\text{th}}$ element equal to $\Phi_{N,m,n} = \exp(-j\pi(1/4 - (m - n)^2/N)/\sqrt{N})$.

Further, given $a_0 \in \mathbb{R}$, $\lfloor a_0 \rfloor = \max\{m \in \mathbb{Z} \mid m \leq a_0\}$, $\lceil a_0 \rceil = \min\{m \in \mathbb{Z} \mid m \geq a_0\}$, and given $b_0, c_0 \in \mathbb{Z}_+$, an interval of integers can be defined as $[b_0, c_0] = \{x \in \mathbb{Z} \mid b_0 \leq x \leq c_0\}$.

II. DISCRETE ORTHONORMAL S-TRANSFORM

As the proposed DMCT builds on the DOST, we shall briefly describe it. The DOST is a unitary time-frequency transform and was first introduced by Stockwell in [23]. It divides the time-frequency plane into different tiles that occupy a given frequency band, called voice, during a given symbol period. This transform can be described as

$$\mathbf{S} = \bar{\mathbf{S}} \mathbf{F}_N, \quad (1)$$

in which $\bar{\mathbf{S}} \in \mathbb{C}^{N \times N}$ is the matrix responsible for making the time-frequency sampling and is a block-diagonal matrix given by

$$\bar{\mathbf{S}} \triangleq \begin{bmatrix} \bar{\mathbf{S}}_0 & \mathbf{0}_{\beta_0 \times \beta_1} & \cdots & \mathbf{0}_{\beta_0 \times \beta_{N_p-1}} \\ \mathbf{0}_{\beta_1 \times \beta_0} & \bar{\mathbf{S}}_1 & \cdots & \mathbf{0}_{\beta_1 \times \beta_{N_p-1}} \\ \vdots & \vdots & \ddots & \vdots \\ \mathbf{0}_{\beta_{N_p-1} \times \beta_0} & \mathbf{0}_{\beta_{N_p-1} \times \beta_1} & \cdots & \bar{\mathbf{S}}_{N_p-1} \end{bmatrix}, \quad (2)$$

wherein N_p is the number of voices, $\beta_p, \forall p \in [0, N_p-1]$, is the size and number of tiles within the p^{th} voice, $\bar{\mathbf{S}}_p \in \mathbb{C}^{\beta_p \times \beta_p}$ is the matrix responsible for digitally processing the signal at the p^{th} voice, and $\sum_{p=0}^{N_p-1} \beta_p = N$. The element in the m^{th} row and k^{th} column of $\bar{\mathbf{S}}_p$ is given by

$$\bar{S}_{p,m,k} = \frac{e^{-j\pi\tau_{p,m}}}{\sqrt{\beta_p}} e^{j\frac{2\pi}{\beta_p}\tau_{p,m}(\nu_p - \lfloor \beta_p/2 \rfloor + k)}, \quad (3)$$

with $m, k \in [0, \beta_p - 1]$. Furthermore, β_p , ν_p , and the vector $\tau_p \in \mathbb{R}^{\beta_p \times 1}$, with entries $\tau_{p,m}$, are the coordination parameters and represent the size, central frequency index, and time indexes of the p^{th} voice, respectively. These coordination parameters define the divisions in the time-frequency plane and thus are chosen according to the desired division of the spectrum, as shown in Fig. 1; further details are postponed to Section II-A.

From (3), it is possible to see that

$$\bar{\mathbf{S}}_p = \Lambda_{S,p} \Lambda_{PS,p} \mathbf{F}_{\beta_p}^\dagger, \quad (4)$$

wherein \mathbf{F}_{β_p} is a β_p -size DFT matrix, $\Lambda_{PS,p}$ is a diagonal matrix whose m^{th} diagonal entry is

$$\Lambda_{PS,p,m} = e^{j\frac{2\pi}{\beta_p}\tau_{p,m}(\nu_p - \lfloor \beta_p/2 \rfloor)}, \quad (5)$$

and $\Lambda_{S,p}$ is a diagonal matrix whose m^{th} diagonal entry is

$$\Lambda_{S,p,m} = e^{-j\pi\tau_{p,m}}. \quad (6)$$

Thus, a vector of time domain symbols $\mathbf{x} \in \mathbb{C}^{N \times 1}$ processed with the DOST results in

$$\begin{aligned} \mathbf{x}_S &= \mathbf{S} \mathbf{x} \\ &= \bar{\mathbf{S}} \mathbf{F}_N \mathbf{x} \\ &= \bar{\mathbf{S}} \mathbf{x}_F \\ &= [(\bar{\mathbf{S}}_0 \mathbf{x}_{F,0})^T \ (\bar{\mathbf{S}}_1 \mathbf{x}_{F,1})^T \ \cdots \ (\bar{\mathbf{S}}_{N_p-1} \mathbf{x}_{F,N_p-1})^T]^T, \end{aligned} \quad (7)$$

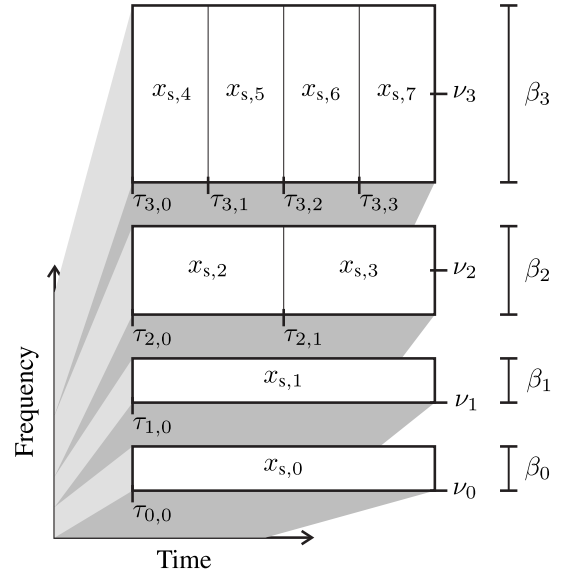


Fig. 1. Illustration of each coordination parameter associated with the voice in the time-frequency plane of the DOST symbol vector with $N = 8$, $\beta_0 = 1$, $\beta_1 = 1$, $\beta_2 = 2$, and $\beta_3 = 4$.

in which $\mathbf{x}_F = \mathbf{F}_N \mathbf{x}$ is the symbol vector in the frequency domain, and $\mathbf{x}_{F,p} = [x_{F,\text{lb}_p} \ x_{F,\text{lb}_p+1} \ \cdots \ x_{F,\text{ub}_p}]^T \in \mathbb{C}^{\beta_p \times 1}$, with $\text{lb}_p = \nu_p - \lfloor \beta_p/2 \rfloor$ and $\text{ub}_p = \nu_p + \lfloor \beta_p/2 \rfloor - 1$. Consequently, we can state that $\mathbf{x}_S = [\mathbf{x}_{S_0}^T \ \mathbf{x}_{S_1}^T \ \cdots \ \mathbf{x}_{S_{N_p-1}}^T]^T$ with

$$\begin{aligned} \mathbf{x}_{S_p} &= \bar{\mathbf{S}}_p \mathbf{x}_{F,p} \\ &= \Lambda_{S,p} \Lambda_{PS,p} \mathbf{F}_{\beta_p}^\dagger \mathbf{x}_{F,p} \end{aligned} \quad (8)$$

and its m^{th} element is equal to

$$\begin{aligned} x_{S_p,m} &= \frac{e^{-j\pi\tau_{p,m}}}{\sqrt{\beta_p}} \sum_{k=\text{lb}_p}^{\text{ub}_p} e^{j\frac{2\pi}{\beta_p}k\tau_{p,m}} x_{F,k} \\ &= \frac{e^{-j\pi\tau_{p,m}}}{\sqrt{N\beta_p}} \sum_{k=\text{lb}_p}^{\text{ub}_p} \sum_{n=0}^{N-1} e^{j\frac{2\pi}{\beta_p}k\tau_{p,m}} e^{-j\frac{2\pi}{N}kn} x_n. \end{aligned} \quad (9)$$

Therefore, the DOST can be summarized in a transform that divides the available bandwidth into voices by applying an N -size DFT followed by N_p β_p -size inverse discrete Fourier transforms (IDFTs). Then it multiplies the divided symbol block in the time domain with the $\Lambda_{PS,p}$ and $\Lambda_{S,p}$ matrices.

A. Coordination Parameters

The process of dividing the available band into voices is controlled by the coordination parameters β_p , ν_p , and τ_p . The first parameter is the voice size, $\beta_p = 2^i$, $i \in \mathbb{N}_+$, it is used to determine the other two parameters and is also the number of tiles, or elements of \mathbf{x}_{S_p} , within the p^{th} voice. Moreover, the values of β_p are determined by a chosen tile geometry¹ of the available bandwidth constrained to

$$\sum_{p=0}^{N_p-1} \beta_p = N. \quad (10)$$

¹In other papers related to the DOST, the tile geometry is called “sampling” [23].

The second parameter, ν_p , is the central frequency index related to the p^{th} voice, given by

$$\nu_p = \sum_{i=0}^{p-1} \beta_i + \lfloor \beta_p/2 \rfloor, \quad (11)$$

whereas the last parameter, represented by

$$\tau_p = [0 \ 1 \ \dots \ \beta_p - 1]^T, \quad (12)$$

is a vector containing the time indexes for the p^{th} voice.

III. DISCRETE MODULAR CHIRP TRANSFORM

The proposed DMCT takes inspiration from the DOST and DFNT to create chirps bounded into different frequency ranges. Section II detailed how the DOST processes a given symbol vector and divides the frequency band into different voices. This process involved an N -size DFT followed by numerous β_p -size IDFT applied in nonoverlapping frequencies. On the other hand, the DFNT creates orthogonal chirps that occupy the whole frequency band.

Let $\mathbf{M} \in \mathbb{C}^{N \times N}$ be the DMCT matrix given by

$$\mathbf{M} = \overline{\mathbf{M}} \mathbf{F}_N, \quad (13)$$

wherein $\overline{\mathbf{M}} \in \mathbb{C}^{N \times N}$ is a block-diagonal matrix defined as

$$\overline{\mathbf{M}} \triangleq \begin{bmatrix} \overline{\mathbf{M}}_0 & \mathbf{0}_{\beta_0 \times \beta_1} & \dots & \mathbf{0}_{\beta_0 \times \beta_{N_p-1}} \\ \mathbf{0}_{\beta_1 \times \beta_0} & \overline{\mathbf{M}}_1 & \dots & \mathbf{0}_{\beta_1 \times \beta_{N_p-1}} \\ \vdots & \vdots & \ddots & \vdots \\ \mathbf{0}_{\beta_{N_p-1} \times \beta_0} & \mathbf{0}_{\beta_{N_p-1} \times \beta_1} & \dots & \overline{\mathbf{M}}_{N_p-1} \end{bmatrix}, \quad (14)$$

in which $\overline{\mathbf{M}}_p \in \mathbb{C}^{\beta_p \times \beta_p}$ digitally processes the signal of the p^{th} voice, creating orthogonal chirps therein. We define the element of the m^{th} row and k^{th} column of $\overline{\mathbf{M}}_p$ as

$$\overline{M}_{p,m,k} \triangleq \frac{1}{\sqrt{\beta_p}} e^{j \frac{2\pi}{\beta_p} \tau_{p,m} (\nu_p - \lfloor \beta_p/2 \rfloor + k)} e^{-j \frac{\pi}{\beta_p} k^2}, \quad (15)$$

wherein $\exp(-j\pi k^2/\beta_p)$ is the k^{th} element of a β_p -size Zadoff-Chu sequence.² This term contrasts with $\exp(-j\pi \tau_{p,m})$ in (3). Note that one has the discrete frequency domain index, k . In contrast, the other has the index of the transform domain,³ m . Hence, the proposed DMCT differs from the DOST by including a further digital processing step in the frequency domain. On the other hand, the DOST comprises an extra digital processing step in the transform domain, which the DMCT lacks.

Consequently, we can write $\overline{\mathbf{M}}_p$ as

$$\overline{\mathbf{M}}_p = \Lambda_{\text{PS},p} \mathbf{F}_{\beta_p}^\dagger \Lambda_{\text{ZC},p}, \quad (16)$$

wherein $\Lambda_{\text{ZC},p}$ is a diagonal matrix whose k^{th} diagonal entry is $\Lambda_{\text{ZC},p,k,k} = \exp(-j\pi k^2/\beta_p)$.

²The Zadoff-Chu sequence is a complex-exponential sequence whose frequencies change linearly over time, maintaining constant amplitude and zero autocorrelation properties.

³The term “transform domain” in this paper refers to the domain where signals, initially in the discrete-time domain, are transformed after being processed by the DMCT.

Moreover, a vector representation of a block of symbols processed with the DMCT is defined as

$$\begin{aligned} \mathbf{x}_M &\triangleq \mathbf{M} \mathbf{x} \\ &= \overline{\mathbf{M}} \mathbf{F}_N \mathbf{x} \\ &= [(\overline{\mathbf{M}}_0 \mathbf{x}_{\text{F},0})^T \ \dots \ (\overline{\mathbf{M}}_{N_p-1} \mathbf{x}_{\text{F},N_p-1})^T]^T \\ &= [\mathbf{x}_{\text{M}_0}^T \ \mathbf{x}_{\text{M}_1}^T \ \dots \ \mathbf{x}_{\text{M}_{N_p-1}}^T]^T, \end{aligned} \quad (17)$$

with \mathbf{x}_{M_p} being given by

$$\mathbf{x}_{\text{M}_p} = \Lambda_{\text{PS},p} \mathbf{F}_{\beta_p}^\dagger \Lambda_{\text{ZC},p} \mathbf{x}_{\text{F},p}, \quad (18)$$

wherein its m^{th} element is equal to

$$\begin{aligned} x_{\text{M},p,m} &= \frac{1}{\sqrt{\beta_p}} \sum_{k=\text{lb}_p}^{\text{ub}_p} e^{j \frac{2\pi}{\beta_p} k \tau_{p,m}} e^{-j \frac{\pi}{\beta_p} k^2} x_{\text{F},k} \\ &= \frac{1}{\sqrt{N \beta_p}} \sum_{k=\text{lb}_p}^{\text{ub}_p} \sum_{n=0}^{N-1} e^{j \frac{2\pi}{\beta_p} k \tau_{p,m}} e^{-j \frac{\pi}{\beta_p} k^2} e^{-j \frac{2\pi}{N} k n} x_n. \end{aligned} \quad (19)$$

Fig. 2(a) outlines how the DMCT acts on a symbol vector \mathbf{x} . First, it applies an N -size DFT to it. The resulting block is split into N_p nonoverlapping β_p -size blocks. Then, each block is multiplied by a diagonal matrix whose main diagonal is given by a Zadoff-Chu sequence to create chirps bounded in their voices. Next, each β_p -size block is multiplied by an IDFT matrix of compatible dimension. Last, all voices pass through a phase shift process. In Fig. 2(b), the time-frequency representation of a symbol vector processed with the DMCT is depicted. Unlike the DOST, where division occurs in both time and frequency domains, in the current context, division occurs only in the frequency domain. This is because the chirps occupy the entire time period, suggesting that the transmitted symbols are suitable for time intervals in which the channel impulse response (CIR) is time-invariant—*i.e.*, within its coherence time. Finally, Fig. 2(c) illustrates the waveform for the first chirp of each voice.

A. The DMCT Unitary Property

From (13) and (14), we can state that \mathbf{M} will be unitary if $\overline{\mathbf{M}}$ is unitary since the DFT already own this property. We have that $\overline{\mathbf{M}} \overline{\mathbf{M}}^\dagger$ and $\overline{\mathbf{M}}^\dagger \overline{\mathbf{M}}$ are block diagonal matrices with the p^{th} matrix diagonal component equal to $\overline{\mathbf{M}}_p \overline{\mathbf{M}}_p^\dagger$ and $\overline{\mathbf{M}}_p^\dagger \overline{\mathbf{M}}_p$, respectively. Consequently,

$$\overline{\mathbf{M}}_p \overline{\mathbf{M}}_p^\dagger = \Lambda_{\text{PS},p} \mathbf{F}_{\beta_p}^\dagger \Lambda_{\text{ZC},p} \Lambda_{\text{ZC},p}^\dagger \mathbf{F}_{\beta_p} \Lambda_{\text{PS},p}^\dagger \quad (20)$$

and

$$\overline{\mathbf{M}}_p^\dagger \overline{\mathbf{M}}_p = \Lambda_{\text{ZC},p}^\dagger \mathbf{F}_{\beta_p} \Lambda_{\text{PS},p}^\dagger \Lambda_{\text{PS},p} \mathbf{F}_{\beta_p}^\dagger \Lambda_{\text{ZC},p}. \quad (21)$$

Since \mathbf{F}_{β_p} is a DFT, $\Lambda_{\text{PS},p} \Lambda_{\text{PS},p}^\dagger = \Lambda_{\text{PS},p}^\dagger \Lambda_{\text{PS},p} = \mathbf{I}_{\beta_p}$, and $\Lambda_{\text{ZC},p} \Lambda_{\text{ZC},p}^\dagger = \Lambda_{\text{ZC},p}^\dagger \Lambda_{\text{ZC},p} = \mathbf{I}_{\beta_p}$, then $\overline{\mathbf{M}}$ and \mathbf{M} are unitary matrices. The unitary property of the DMCT ensures that the inverse discrete modular chirp transform (IDMCT) is given by the complex transpose of the DMCT or, in short, by \mathbf{M}^\dagger .

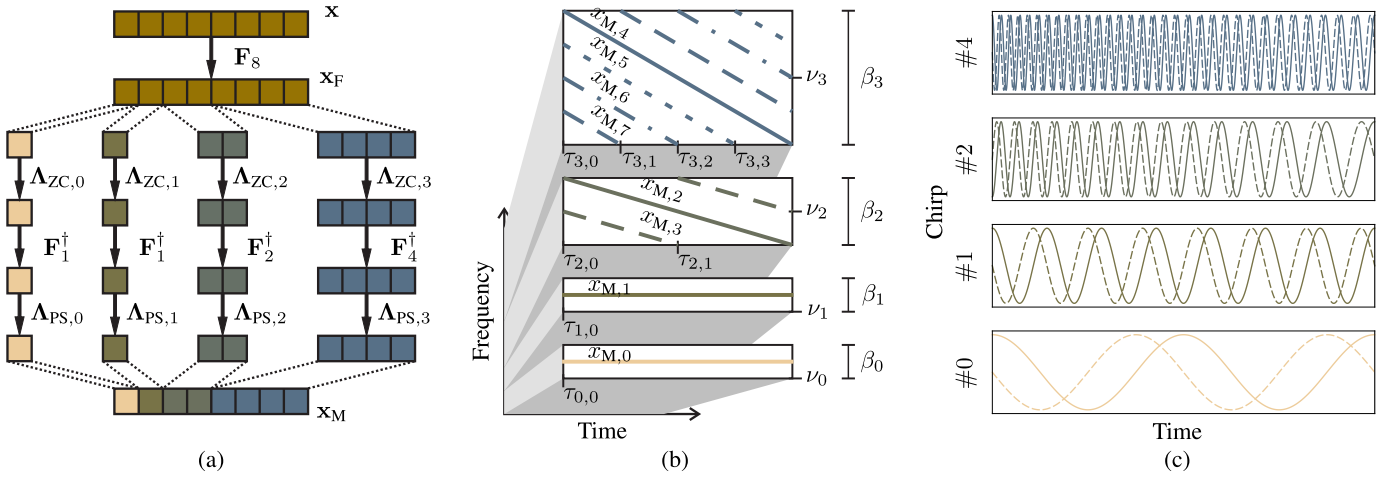


Fig. 2. Illustration of (a) the DMCT process; and how it relates to (b) the time-frequency representation of the DMCT symbol vector; (c) the in-phase (solid) and the quadrature (dashed) components of the chirps created in (a). (inspired by [26].)

B. Tile Geometry

As mentioned earlier, the coordination parameters β_p , ν_p , and τ_p play an important role both in defining how the DMCT divides the band into voices and in creating the orthogonality between chirps from the same and different voices. To build the tile geometry of this transform, first, it is necessary to define the values of β_p , $\forall p \in [0, N_p - 1]$. This paper only considers dyadic values of β_p that follow the constraint imposed by (10). Once the values of β_p are chosen for all p , then ν_p and τ_p can be derived using (11) and (12), respectively. Following this, one may design the DMCT to divide the band as one wishes. However, an appropriate tile geometry can simplify the DMCT equations by transforming the matrix $\Lambda_{PS,p}$ in a neutral product element, meaning that it will be equal to an identity matrix for every p . We name such a tile geometry as *regular geometry*, whose definition is as follows:

Definition 1 (Regular Tile Geometry): It is a set of β_p , with $p \in [0, N_p - 1]$ and $\sum_{p=0}^{N_p-1} \beta_p = N$, for which the condition

$$\frac{\nu_p - \lfloor \beta_p/2 \rfloor}{\beta_p} \in \mathbb{N} \quad (22)$$

is satisfied for all $\beta_p > 1$.⁴

If a regular tile geometry is assumed, $\Lambda_{PS,p} = \mathbf{I}_{\beta_p}$ and, as a consequence, the DMCT window matrix, $\bar{\mathbf{M}}$, is reduced to a block-diagonal matrix with the p^{th} matrix component given by

$$\bar{\mathbf{M}}_p = \mathbf{F}_{\beta_p}^\dagger \Lambda_{ZC,p}. \quad (23)$$

In this regard, this section presents some prebuilt regular geometries, which are based on well-established techniques for time-frequency division.

1) *Uniform*: The straightforward division of the band characterizes the Uniform tile geometry into N_p voices of equal size, in which $N_p \leq N$. This tile geometry is inspired by the short-time Fourier transform, which presents a fixed time-frequency resolution [27]. Consequently, we have

$$\beta_p = \frac{N}{N_p}, \quad (24)$$

⁴A voice p with $\beta_p = 1$ will always generate $\Lambda_{PS,p} = [1]$ since $\tau_p = [0]$.

and

$$\nu_p = p \frac{N}{N_p} + \left\lfloor \frac{N}{2N_p} \right\rfloor, \quad (25)$$

which results in $(\nu_p - \lfloor \beta_p/2 \rfloor)/\beta_p = p$ and $\Lambda_{PS,p} = \mathbf{I}_{\beta_p}$, $\forall p$. Furthermore, we also can state that the DMCT can be interpreted as a transform that combines the DFT and DFnT. Indeed, we can consider that the DFT and DFnT are special cases of a Uniform tile geometry applied to the DMCT as follows:

- **DFT**: Let us consider that $N_p = N$, which makes $\beta_p = 1$, $\forall p$. This implies $\bar{\mathbf{M}}_p = [1]$, $\forall p$. Therefore, the window matrix becomes a diagonal matrix with elements equal to 1, i.e., $\bar{\mathbf{M}} = \mathbf{I}_N$, and, as a consequence, $\mathbf{M} = \mathbf{I}_N \mathbf{F}_N$.
- **DFnT**: When we consider a single voice scenario, i.e., $N_p = 1$, with size $\beta_0 = N$, the window matrix $\bar{\mathbf{M}}$ will no longer be a block diagonal matrix. It will act as a Zadoff-Chu sequence followed by an IDFT, both of size N , resulting in $\mathbf{M} = \mathbf{F}_N^\dagger \Lambda_{ZC,0} \mathbf{F}_N$, which is equal to the DFnT matrix.

Fig. 3(a) illustrates the time-frequency plane for a Uniform tile geometry with $N = 8$ and $N_p = 4$.

2) *Octave*: The Octave tile geometry consists of a geometric progression for the voice size, doubling it for each subsequent voice. The dyadic decomposition of the time-frequency plane commonly used by the wavelet transform is equivalent to this tile geometry, in which the frequency resolution is poor for high-frequency and good for low-frequency contents [27], [28]. In this sense, we have $N_p = \log_2(N) + 1$ and

$$\beta_p = \begin{cases} 1 & \text{for } p = 0 \\ 2^{p-1} & \text{for } 1 \leq p \leq N_p - 1, \end{cases} \quad (26)$$

leading to

$$\nu_p = \begin{cases} 0 & \text{for } p = 0 \\ 1 & \text{for } p = 1 \\ 2^{p-1} + 2^{p-2} & \text{for } 2 \leq p \leq N_p - 1, \end{cases} \quad (27)$$

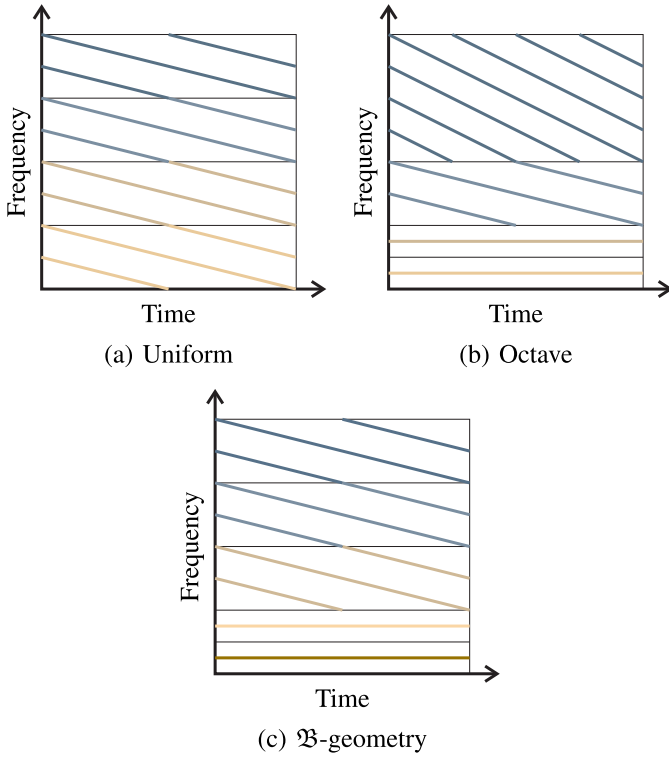


Fig. 3. Illustration of the time-frequency plane for Uniform, Octave, and \mathcal{B} tile geometries.

resulting in $(\nu_p - \lfloor \beta_p/2 \rfloor)/\beta_p = 1$ and $\Lambda_{\text{PS},p} = \mathbf{I}_{\beta_p}$, for $p > 1$. Fig. 3(b) illustrates the time-frequency plane when an Octave tile geometry is adopted.

3) \mathcal{B} -Geometry: The \mathcal{B} -geometry was proposed in [24] to be used by multicarrier techniques based on DOST to balance the complexity of CSI feedback associated with resource allocation and data rate loss. It also has a β_p that increases for each consecutive voice until it reaches a size limit, given by $\mathcal{B} = 2^\alpha$, $\alpha \in \mathbb{N}$. The \mathcal{B} -geometry presents the number of voices equal to

$$N_p = N/2^\alpha + \alpha \quad (28)$$

while the voice size, β_p , is given by

$$\beta_p = \begin{cases} 1 & \text{for } p = 0 \\ 2^{p-1} & \text{for } 1 \leq p \leq \alpha \\ 2^\alpha & \text{for } \alpha < p \leq N_p - 1. \end{cases} \quad (29)$$

and, as a consequence, we have

$$\nu_p = \begin{cases} 0 & \text{for } p = 0 \\ 1 & \text{for } p = 1 \\ 2^{p-1} + 2^{p-2} & \text{for } 2 \leq p \leq \alpha \\ (p - \alpha)2^\alpha + 2^{\alpha-1} & \text{for } \alpha < p \leq N_p - 1. \end{cases} \quad (30)$$

Hence, $(\nu_p - \lfloor \beta_p/2 \rfloor)/\beta_p = 1$ for $1 < p \leq \alpha$, $(\nu_p - \lfloor \beta_p/2 \rfloor)/\beta_p = p - \alpha$ for $\alpha < p \leq N_p - 1$, and $\Lambda_{\text{PS},p} = \mathbf{I}_{\beta_p}$, $\forall p$. Fig. 3(c) illustrates the time-frequency plane when the \mathcal{B} -geometry is adopted.

IV. THE OCFDM TECHNIQUE

This section introduces the OCFDM. This technique uses the proposed DMCT, presented in Section III, to split the available frequency band into voices and fill them with chirps. Fig. 4 illustrates the discrete baseband complex OCFDM data communication technique, comprising the transmitter, communication medium modeled by a time-invariant system corrupted by the presence of additive noise, and the receiver.⁵

First, the data bits pass through a modulation process, such as quadrature amplitude modulation (QAM), in which they are mapped into the complex numbers of a given constellation. As a result, we have a block of N parallel modulated symbols arranged into $\mathbf{x}_M \in \mathbb{C}^{N \times 1}$. Next, the modulated symbol block is processed by the IDMCT matrix \mathbf{M}^\dagger , resulting in an N -length symbol block in the discrete-time domain

$$\mathbf{x} = \mathbf{M}^\dagger \mathbf{x}_M. \quad (31)$$

The last step at the transmitter side is to prepend an L_{CP} -length CP to $\mathbf{x} \in \mathbb{C}^{N \times 1}$.

Subsequently, the analog version of every transmitted symbol block is subjected to a channel characterized as LTI. Additive noise in the receiver input is also considered. The assumption of a time-invariant channel is justified by the significantly shorter transmission time for an N -length block symbol compared to the channel coherence time. To model this channel, we consider a vector representation given by $\mathbf{h} = [h[0] \dots h[L_h - 1]]^T$, with $h[n]$ being the n^{th} sample of the CIR and L_h denoting the CIR length. Also, we are considering $L_{\text{CP}} \geq L_h - 1$ and perfect synchronization at the receiver to avoid intersymbol interference (ISI).

The CP is first removed at the receiver side. Consequently, the received block symbol is then given by

$$\mathbf{y} = \mathbf{C}_h \mathbf{x} + \mathbf{v}, \quad (32)$$

wherein $\mathbf{v} \in \mathbb{C}^{N \times 1}$ represents the additive noise vector and \mathbf{C}_h is the CIR circular convolution matrix.

To mitigate the channel effect in the received signal, a frequency domain equalization (FDE) is performed via the matrix \mathbf{E} by applying $\mathbf{F}_N \mathbf{E} \mathbf{F}_N^\dagger$ to the received signal. The FDE is followed by the matrix \mathbf{M} . In this way, we avoid the execution of a pair of direct and inverse DFTs, simplifying the receiver. Therefore, the reconstructed block symbol is given by

$$\begin{aligned} \hat{\mathbf{x}}_M &= \mathbf{M} \mathbf{F}_N^\dagger \mathbf{E} \mathbf{F}_N \mathbf{y} \\ &= \overline{\mathbf{M}} \mathbf{E} \mathbf{F}_N \mathbf{y}, \end{aligned} \quad (33)$$

which can be rewritten as

$$\hat{\mathbf{x}}_M = \overline{\mathbf{M}} \mathbf{E} \mathbf{F}_N \mathbf{C}_h \mathbf{F}_N^\dagger \overline{\mathbf{M}}^\dagger \mathbf{x}_M + \overline{\mathbf{M}} \mathbf{E} \mathbf{F}_N \mathbf{v}. \quad (34)$$

Since \mathbf{C}_h is a circulant matrix, $\mathbf{F}_N \mathbf{C}_h \mathbf{F}_N^\dagger$ will result in a diagonal matrix denoted by Λ_{hf} . The elements in the main diagonal of such a matrix are obtained from the vector $\mathbf{h}_F = \sqrt{N} \mathbf{F}_N [\mathbf{h}^T \mathbf{0}_{(N-L_h) \times 1}^T]^T \in \mathbb{C}^{N \times 1}$, which represents the channel frequency response (CFR) of the

⁵The OCFDM can also be cast as a precoded OFDM, with $\overline{\mathbf{M}}$ being a channel-independent unitary precoding matrix; see [29].

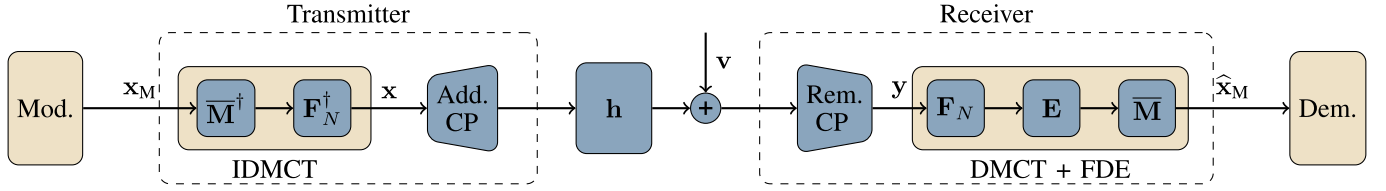


Fig. 4. OCFDM-based data communication technique.

zero-padded version of the CIR. Adopting, for instance, a zero-forcing (ZF) equalization, $\mathbf{E} = \mathbf{\Lambda}_{\mathbf{h}_F}^{-1}$, the reconstructed block symbol will be given by

$$\begin{aligned}\hat{\mathbf{x}}_M &= \bar{\mathbf{M}}\mathbf{\Lambda}_{\mathbf{h}_F}^{-1}\mathbf{\Lambda}_{\mathbf{h}_F}\bar{\mathbf{M}}^\dagger \mathbf{x}_M + \bar{\mathbf{M}}\mathbf{\Lambda}_{\mathbf{h}_F}^{-1}\mathbf{F}_N \mathbf{v} \\ &= \mathbf{x}_M + \bar{\mathbf{M}}\mathbf{\Lambda}_{\mathbf{h}_F}^{-1}\mathbf{v}_F,\end{aligned}\quad (35)$$

where $\mathbf{v}_F \in \mathbb{C}^{N \times 1}$ is the noise vector in the discrete-frequency domain.

At this point, the reconstructed block symbol $\hat{\mathbf{x}}_M$ is injected into the demodulator. In this stage, the elements of the reconstructed block symbol individually pass through a maximum *a posteriori* detector, which provides estimates of the transmitted data bits based on the received complex signals.

A. Computational Complexity

The computational complexity of the OCFDM technique is in Table I alongside the OFDM, OCDM, and OTFDM ones. Both OFDM and OCDM can be derived from the OCFDM, whereas the OTFDM is a data communication technique whose main operator is the DOST, which is the basis transform for the DMCT. The computational complexity is in the number of basic operations (products and sums) for the transmitter and receiver of each data communication technique. It considers direct and inverse transforms for each technique plus the ZF equalization. Other components that do not require basic operations, like the addition and removal of cyclic prefixes, were not considered. For the OCDM, the transmitter uses the fast form of the transform, and the receiver is the usual merge between the DFNT and FDE; hence, the transmitter is given by one DFT and two diagonal matrices while the receiver by two DFTs and diagonal matrices, all N -sized. As a final remark, for the OCFDM and OTFDM, it was considered the computational complexity for the geometries presented in Section III-B and the process depicted in Fig. 2 and in [24]. It is noticeable that both of them possess the same computational complexity.

B. Data Rate and Resource Allocation

This section aims to elucidate how the frequency division created by the DMCT can enable resource allocation in OCFDM. To this end, it is convenient to derive the SNR that each chirp experiences in the OCFDM technique and then its data rate. From (35), we can state that $\hat{\mathbf{x}}_M = [\hat{\mathbf{x}}_{M_0}^T \hat{\mathbf{x}}_{M_1}^T \dots \hat{\mathbf{x}}_{M_{N_p-1}}^T]^T$, in which $\hat{\mathbf{x}}_{M_p} = [\hat{x}_{M,lb_p} \hat{x}_{M,lb_p+1} \dots \hat{x}_{M,ub_p}]^T \in \mathbb{C}^{\beta_p \times 1}$ is the vector

TABLE I
COMPUTATIONAL COMPLEXITY FOR THE OFDM, OCDM, AND OCFDM

Transmitter	
Technique	Number of products
OFDM	$2N \log_2(N)$
OCDM	$2N \log_2(N) + 2N$
OTFDM	$2N \log_2(N) + \sum_{p=0}^{N_p-1} 2\beta_p \log_2(\beta_p) + N$
OCFDM	$2N \log_2(N) + \sum_{p=0}^{N_p-1} 2\beta_p \log_2(\beta_p) + N$
Technique	Number of sums
OFDM	$3N \log_2(N)$
OCDM	$3N \log_2(N)$
OTFDM	$3N \log_2(N) + \sum_{p=0}^{N_p-1} 3\beta_p \log_2(\beta_p)$
OCFDM	$3N \log_2(N) + \sum_{p=0}^{N_p-1} 3\beta_p \log_2(\beta_p)$
Receiver	
Technique	Number of products
OFDM	$2N \log_2(N) + N$
OCDM	$4N \log_2(N) + 2N$
OTFDM	$2N \log_2(N) + \sum_{p=0}^{N_p-1} 2\beta_p \log_2(\beta_p) + 2N$
OCFDM	$2N \log_2(N) + \sum_{p=0}^{N_p-1} 2\beta_p \log_2(\beta_p) + 2N$
Technique	Number of sums
OFDM	$3N \log_2(N)$
OCDM	$6N \log_2(N)$
OTFDM	$3N \log_2(N) + \sum_{p=0}^{N_p-1} 3\beta_p \log_2(\beta_p)$
OCFDM	$3N \log_2(N) + \sum_{p=0}^{N_p-1} 3\beta_p \log_2(\beta_p)$

of reconstructed chirps within the p^{th} voice, with

$$\hat{\mathbf{x}}_{\bar{M}_p} = \mathbf{x}_{\bar{M}_p} + \bar{\mathbf{M}}_p \mathbf{\Lambda}_{\mathbf{h}_{F,p}}^{-1} \mathbf{v}_{F,p}, \quad (36)$$

wherein $\mathbf{v}_{F,p} = [v_{F,lb_p} \ v_{F,lb_p+1} \ \dots \ v_{F,ub_p}]^T \in \mathbb{C}^{\beta_p \times 1}$ and $\mathbf{\Lambda}_{\mathbf{h}_{F,p}}$ is a diagonal matrix with deterministic elements equal to $\mathbf{h}_{F,p} = [h_{F,lb_p} \ h_{F,lb_p+1} \ \dots \ h_{F,ub_p}]^T \in \mathbb{C}^{\beta_p \times 1}$, which is the CFR of the channel related to the p^{th} voice. Therefore, the m^{th} chirp within the p^{th} voice is given by

$$\begin{aligned}\hat{x}_{\bar{M}_p,m} &= x_{\bar{M}_p,m} + \frac{1}{\sqrt{\beta_p}} \sum_{k=lb_p}^{ub_p} e^{j\frac{2\pi}{\beta_p} \tau_{p,m} k} e^{-j\frac{\pi}{\beta_p} \tau_{p,k}^2} \Lambda_{\mathbf{h}_{F,p}}^{-1} v_{F,k}.\end{aligned}\quad (37)$$

When considering the modulated signal and noise as random signals, we can interpret the reconstructed signal $\hat{\mathbf{x}}_{\bar{M}_p,m}$ as a

realization of the following random variable (for a given m):

$$\begin{aligned} \hat{\mathcal{X}}_{\bar{M}_p, m} &= \mathcal{X}_{\bar{M}_p, m} + \frac{1}{\sqrt{\beta_p}} \sum_{k=\text{lb}_p}^{\text{ub}_p} e^{j \frac{2\pi}{\beta_p} \tau_{p, m} k} e^{-j \frac{\pi}{\beta_p} \tau_{p, m}^2 k} \Lambda_{h_F, k, k}^{-1} \mathcal{V}_{F, k}, \end{aligned} \quad (38)$$

in which $\mathcal{X}_{\bar{M}_p, m}$ and $\mathcal{V}_{F, k}$ are uncorrelated random variables with realizations $x_{\bar{M}_p, m}$ and $v_{F, k}$, respectively, for each $k \in [\text{lb}_p, \text{ub}_p]$. Furthermore, we assume $\mathbb{E}\{\mathcal{V}_{F, k}\} = 0$, $\forall k$, and $\mathbb{E}\{\mathcal{V}_{F, k} \mathcal{V}_{F, i}^*\} = 0$, $\forall k \neq i$. The noise power at the k^{th} frequency index is $\mathbb{E}\{\mathcal{V}_{F, k} \mathcal{V}_{F, k}^*\} = P_{v, k}$. Consequently, the SNR associated with the m^{th} chirp of the p^{th} voice is given by

$$\gamma_{p, m} = \frac{P_{x_{\bar{M}_p, m}}}{\frac{1}{\beta_p} \sum_{k=\text{lb}_p}^{\text{ub}_p} |\Lambda_{h_F, k, k}^{-1}|^2 P_{v, k}}, \quad (39)$$

wherein $P_{x_{\bar{M}_p, m}} = \mathbb{E}\{\mathcal{X}_{\bar{M}_p, m} \mathcal{X}_{\bar{M}_p, m}^*\}$ is the signal power. Moreover, the nSNR, which is defined by

$$\bar{\gamma}_{p, m} = \frac{\gamma_{p, m}}{P_{x_{\bar{M}_p, m}}}, \quad (40)$$

can be expressed as

$$\bar{\gamma}_{p, m} = \left(\frac{1}{\beta_p} \sum_{k=\text{lb}_p}^{\text{ub}_p} \dot{\gamma}_k^{-1} \right)^{-1}, \quad (41)$$

in which $\dot{\gamma}_k = |\Lambda_{h_F, k, k}|^2 / P_{v, k}$ is the nSNR of the k^{th} frequency index, which is the nSNR for the k^{th} subcarrier for the OFDM technique. In other words, the nSNR for the p^{th} voice is a harmonic mean of $\dot{\gamma}_k$ for $k \in [\text{lb}_p, \text{ub}_p]$, which is equal to what is obtained using OTFDM [24].

From (41), it is noticeable that the nSNR is directly related to the voice size and its central frequency index and does not change between the chirps of the same voice. Thus, we can omit the index m from $\bar{\gamma}_{p, m}$, defining the nSNR per voice $\bar{\gamma}_p = \bar{\gamma}_{p, m}$. The nSNR may differ from one voice to another depending only on the CFR and noise statistics. This is different from what happens in OCDM, in which the nSNR for all chirps is given by the harmonic mean of $\dot{\gamma}_k$, $k \in [0, N-1]$, i.e., [8], [20]

$$\dot{\gamma} = \left(\frac{1}{N} \sum_{k=0}^{N-1} \dot{\gamma}_k^{-1} \right)^{-1}. \quad (42)$$

Interestingly, this expression can be rewritten as

$$\dot{\gamma} = \left(\sum_{p=0}^{N_p-1} \frac{\beta_p}{N} \frac{1}{\beta_p} \sum_{k=\text{lb}_p}^{\text{ub}_p} \dot{\gamma}_k^{-1} \right)^{-1} \quad (43)$$

$$= \left(\sum_{p=0}^{N_p-1} \frac{\beta_p}{N} \bar{\gamma}_p^{-1} \right)^{-1}, \quad (44)$$

that is, the OCDM's nSNR is given by the weighted harmonic mean of the OCFDM's nSNRs, $\bar{\gamma}_p$, with weights β_p/N , so that $\sum_{p=0}^{N_p-1} \beta_p/N = 1$.

A data rate for both OCFDM and OCDM can be obtained under the same assumptions and as a function of their respective nSNRs. By disregarding the noise correlation, the data rate expression⁶ for the OCFDM is as follows:

$$R_M = \frac{B}{N + L_{CP}} \sum_{p=0}^{N_p-1} \sum_{m=0}^{\beta_p-1} \log_2 \left(1 + \frac{P_{x_{\bar{M}_p, m}} \bar{\gamma}_p}{\Gamma} \right), \quad (45)$$

wherein Γ is the SNR gap, which is a constant considering a large M , and B is the frequency bandwidth. As for the OCDM's, one similarly has

$$R_C = \frac{B}{N + L_{CP}} \sum_{n=0}^{N-1} \log_2 \left(1 + \frac{P_{x_{c, n}} \dot{\gamma}}{\Gamma} \right), \quad (46)$$

in which $P_{x_{c, n}}$ is the power of the n^{th} OCDM chirp and $\dot{\gamma}$ is its nSNR.

When $P_{x_{c, n}} \dot{\gamma}/\Gamma \gg 1$ and $P_{x_{\bar{M}_p, m}} \bar{\gamma}_p/\Gamma \gg 1$, and when for each n there exists a pair (p, m) such that $P_{x_{c, n}} = P_{x_{\bar{M}_p, m}}$, meaning that we are using the same power allocation for both systems, then (45) and (46) can be respectively approximated as follows:

$$R_M \approx \frac{B}{N + L_{CP}} \log_2 \left(\prod_{p=0}^{N_p-1} \prod_{m=0}^{\beta_p-1} \frac{P_{x_{\bar{M}_p, m}} \bar{\gamma}_p}{\Gamma} \right), \quad (47)$$

and

$$R_C \approx \frac{B}{N + L_{CP}} \log_2 \left(\prod_{n=0}^{N-1} \frac{P_{x_{c, n}} \dot{\gamma}}{\Gamma} \right), \quad (48)$$

in which

$$\prod_{n=0}^{N-1} \frac{P_{x_{c, n}}}{\Gamma} = \prod_{p=0}^{N_p-1} \prod_{m=0}^{\beta_p-1} \frac{P_{x_{\bar{M}_p, m}}}{\Gamma}. \quad (49)$$

Given weights β_p/N , $\sum_{p=0}^{N_p-1} \beta_p/N = 1$, we know that the weighted geometric mean of $\bar{\gamma}_p$ with weights β_p/N , is greater or equal to⁷ the weighted harmonic mean of $\bar{\gamma}_p$, i.e., [30]

$$\prod_{p=0}^{N_p-1} \bar{\gamma}_p^{\frac{\beta_p}{N}} \geq \left(\sum_{p=0}^{N_p-1} \frac{\beta_p}{N} \bar{\gamma}_p^{-1} \right)^{-1}, \quad (50)$$

which, together with (43), (47), and (48), imply that the OCFDM attains equal or greater data rate than the OCDM for sufficiently high SNR, i.e.,

$$R_M \geq R_C \quad (\text{asymptotically}). \quad (51)$$

Furthermore, the variation between the nSNR of each voice attained by the OCFDM allows the implementation of algorithms to allocate power/bit among different voices and chirps for a given objective function. In this sense, let us consider a resource allocation problem that aims to maximize the data rate in (45) by allocating power to each chirp under sum power constraint (SPC). This constraint limits the overall transmission power, i.e., the power the transmitter uses across

⁶We do not analyze the maximum information rate of the systems here.

⁷Equality holds when $\bar{\gamma}_p$, $\forall p$, is constant.

all voices and chirps. In this case, the resource allocation problem is formulated as follows:

$$\underset{P_{\mathbf{x}_{\mathbf{M},p,m}}}{\text{maximize}} \quad R_{\mathbf{M}} \quad (52)$$

$$\text{subject to} \quad \sum_{p=0}^{N_p-1} \sum_{m=0}^{\beta_p-1} P_{\mathbf{x}_{\mathbf{M},p,m}} \leq P_{\mathbf{T}} \quad (\text{SPC})$$

$$P_{\mathbf{x}_{\mathbf{M},p,m}} \geq 0, \quad \forall p, m. \quad (53)$$

This optimization problem resembles the well-known problem of maximizing the information rate of a set of N parallel independent channels, in which the solution is given by the famous water-filling algorithm [31]. In our case, which is to maximize the data rate in (45), we can use the water-filling algorithm to allocate the transmission power based on Γ and the nSNR of each OCFDM chirp. If an additional set of constraints is included in (53), restricting the allocated power to fractional numbers, a greedy algorithm, like the one proposed by Levin-Campello [21], can be used to solve this optimization problem.

Since all chirps within the same voice have equal nSNRs, the power allocated to all chirps of that voice will be equal, such that $P_{\mathbf{x}_{\mathbf{M},p,m}} = P_{\mathbf{x}_{\mathbf{M},p}}, \forall m$. Consequently, (45) can be rewritten as

$$R_{\mathbf{M}} = \frac{B}{N + L_{\text{CP}}} \sum_{p=0}^{N_p-1} \beta_p \log_2 \left(1 + \frac{P_{\mathbf{x}_{\mathbf{M},p}} \bar{\gamma}_p}{\Gamma} \right). \quad (54)$$

This expression allows us to understand how the frequency division introduced by the DMCT enables resource allocation in chirp-based multicarrier techniques. If the OCDM is considered, then $\beta_p = N$, $N_p = 1$, and the summation in (46) is reduced to a single term. This means there is a single voice, and the nSNR is the same for all chirps. Consequently, there is no degree of freedom to distribute the available transmission power fairly. On the other hand, as the OCFDM technique is assumed, the transmission power can be allocated to different voices according to their CFR and the power spectral density (PSD) of the additive noise.

C. Shaping the OCFDM

In Section III-B, we presented the concept of regular geometry and how it creates different patterns of frequency division within the band. When designing and choosing one of the geometries from Section III-B, one may focus on the following three parameters: the maximum number of frequency divisions, N , the number of voices, N_p , and the maximum voice size, β_{\max} . Note that $\beta_{\max} = \beta_p, \forall p$, for the Uniform geometry and $\beta_{\max} = \mathfrak{B}$ for the \mathfrak{B} -geometry.

The Octave geometry offers the least flexibility of the three geometries considered, relying solely on the block-size N . It means that, for a given N , the Octave geometry produces only one frequency division pattern that will always prioritize the SER over data rate performance. In contrast, the Uniform and \mathfrak{B} -geometry require the specification of one additional parameter, either the number of voices or the maximum voice size. These parameters, N_p and β_{\max} , respectively, are

TABLE II
TILE GEOMETRY GUIDELINE

Design factor	Geometry	Prioritized KPI
N_p	Uniform	Data Rate
	\mathfrak{B} -geometry	SER, robustness to interference
β_{\max}	Uniform	SER, robustness to interference
	\mathfrak{B} -geometry	Data Rate

interdependent in the context of the Uniform and \mathfrak{B} -geometry, meaning that selecting one determines the value of the other as shown in (24) and (28). Furthermore, the increase of one results in the decrease of the other.

In frequency selective channels, the voice size is the resource that directly impacts the nSNR, and, consequently, the following key-performance indicators (KPIs): SER, robustness to interference, and data rate. In this context, if a single voice occupies a subband, the chirps in that subband would experience better SER performance and greater robustness to interference compared to a scenario where multiple voices occupy the same subband. This scenario reflects the asymptotic case of SER optimization generated through a power allocation that results in a uniform SNR [32]. On the other hand, the case with multiple voices occupying that subband is analogous to the OCFDM, presenting an asymptotic data rate higher than the OCDM's, as proved in Section IV-B.

Therefore, if the defining factor for designing the OCFDM is N_p , the Uniform geometry will prioritize data rate performance. In contrast, the \mathfrak{B} -geometry will prioritize SER and robustness to interference, assuming both geometries employ the same N_p . On the other hand, if we base our design on β_{\max} , the Uniform geometry will exhibit better SER performance and robustness to interference. In contrast, the \mathfrak{B} -geometry will offer a higher data rate when both geometries employ the same β_{\max} . Table II summarizes these points.

V. NUMERICAL RESULTS

This section assesses the performance of the OCFDM while comparing it with other multicarrier techniques, such as the OFDM, OCDM [6], and OTFDM [24]. Note that the AFDM is omitted because its performance equals the OCDM's for LTI channels since the parameter tuning of the DAFT leads to the DFNT for time-invariant scenarios [18]. The KPIs for the numerical experiments are nSNR, uncoded SER in perfect conditions and with interference, coded BER, peak-to-average power ratio (PAPR), and data rate with and without power allocation technique, *i.e.*, water-filling algorithm [31].

To this end, we considered an ensemble of wireless channels accounting for both small- and large-scale fading effects. The small-scale fading was derived from the IEEE 802.15.4a channel model considering the line-of-sight (LOS) residential environment [33], [34]. We disregarded the frequency dependence of antennas and considered a bandwidth $B = 80$ MHz in the frequency band around 5 GHz with $N = 2048$ sub-carriers/chirps [35]. As for large-scale fading, we assumed a

log-distance path loss model without shadowing, as described by [36]. The distance between the transmitter and receiver was assumed to be 7 m, whereas the path loss exponent and the path loss at a reference distance were obtained from [37], considering the LOS condition. These parameters resulted in a large-scale path loss of 59.03 dB. All the resulting CIRs can be suitably represented with $L_h = 12$. A different channel realization was selected for each Monte Carlo run. The Monte Carlo simulation was performed over 100 different wireless channels, and we computed the median value of each KPI in our final results.

Regarding the noise, our numerical simulations considered a model of a circularly symmetric complex additive white Gaussian noise (CAWGN) with PSD equal to -173.8 dBm/Hz. Moreover, the receiver was assumed to have a noise figure equal to 3.3 dB [37], which implies $P_{V,k} = -124.58$ dBm, $\forall k$.

A. Tile Geometry and nSNR Comparisons

In Section IV-B, we showed that the nSNR may change from one voice to another depending on β_p and ν_p , but also on the CFR and noise statistics of the voice. Therefore, OCFDM performance may change for different geometries, making the choice of tile geometry utterly important. From the three regular geometries in Section III-B, the Octave presents a rigid tile geometry that depends only on N , while the other two yield multiple setups for the same number of chirps N . Thus, this section analyzes the geometries used in the numerical simulations.

The numerical simulations used the Uniform tile geometry with $N_p = 16$, the 256-geometry, and the Octave. This geometry configuration results in the Uniform and 256-geometry presenting the same number of voices. Therefore, we could expect that the Uniform geometry would exhibit a better data rate, while the 256-geometry would attain better SER and greater robustness to interference (see Section IV-C). Table III lists the chirps and the bandwidth related to each voice, B_p , of each tile geometry. The differences between adopting those geometries are evident from the spectrum occupancy perspective. The voices associated with the Octave tile geometry kept growing exponentially, causing the voice $p = 11$ to occupy half of the total bandwidth, or $B_{11} = 40$ MHz. On the other hand, the Uniform tile geometry had all voices with an equal number of chirps, 128, and bandwidth, $B_p = 5$ MHz. As for the 256-geometry, which is a part Octave and part Uniform tile geometry, it followed the exponential growth of voices until reaching a size of 256 (*i.e.*, a bandwidth of 10 MHz) at $p = 9$; then it kept the same size for the subsequent voices.

The tile geometry directly influences the division of the frequency band, thereby impacting the nSNR of the OCFDM technique. In this regard, Fig. 5 depicts the $\text{nSNR} \times \text{chirp/subcarrier index}$ for the OCFDM, with each tile geometry from Table III taken into consideration, as well as for the OFDM and OCDM techniques. For the OFDM, the nSNR follows the channel and noise characteristics of each subband, changing for every subcarrier. On the other hand, the nSNR is

TABLE III
TILE GEOMETRY SETUPS

Octave				
Voice(p)	Chirps(#)	B_p (MHz)		
0	0	0.04		
1	1	0.04		
2	2 – 3	0.08		
3	4 – 7	0.16		
4	8 – 15	0.31		
5	16 – 31	0.62		
6	32 – 63	1.25		
7	64 – 127	2.50		
8	128 – 255	5.00		
9	256 – 511	10.00		
10	512 – 1023	20.00		
11	1024 – 2047	40.00		

Uniform			256-geometry	
Voice(p)	Chirps(#)	B_p (MHz)	Chirps(#)	B_p (MHz)
0	0 – 127	5.00	0	0.04
1	128 – 255	5.00	1	0.04
2	256 – 383	5.00	2 – 3	0.08
3	384 – 511	5.00	4 – 7	0.16
4	512 – 639	5.00	8 – 15	0.31
5	640 – 767	5.00	16 – 31	0.62
6	768 – 895	5.00	32 – 63	1.25
7	896 – 1023	5.00	64 – 127	2.50
8	1024 – 1151	5.00	128 – 255	5.00
9	1152 – 1279	5.00	256 – 511	10.00
10	1280 – 1407	5.00	512 – 765	10.00
11	1408 – 1535	5.00	768 – 1023	10.00
12	1536 – 1663	5.00	1024 – 1279	10.00
13	1664 – 1791	5.00	1280 – 1535	10.00
14	1792 – 1919	5.00	1536 – 1791	10.00
15	1920 – 2047	5.00	1792 – 2047	10.00

constant for the OCDM since it is the harmonic mean of the channel-to-noise gains of all subbands [8]. Also, according to Section III-B, the OCDM and OFDM are equivalent to the OCFDM with Uniform tile geometry with $N_p = 1$ and $N_p = N$, respectively.

For the OCFDM, each tile geometry presented a different nSNR profile. Indeed, each shows a unique interpretation of the channel resource in terms of nSNR by the OCFDM. For instance, a tile geometry with a set of smaller-sized voices, such as Uniform considered in this section, presented an nSNR that tends to follow the channel-to-noise gain related to using the OFDM technique. In contrast, the nSNR of tile geometry with larger-sized voices, such as the Octave, tends to flatten the nSNR for the channel.

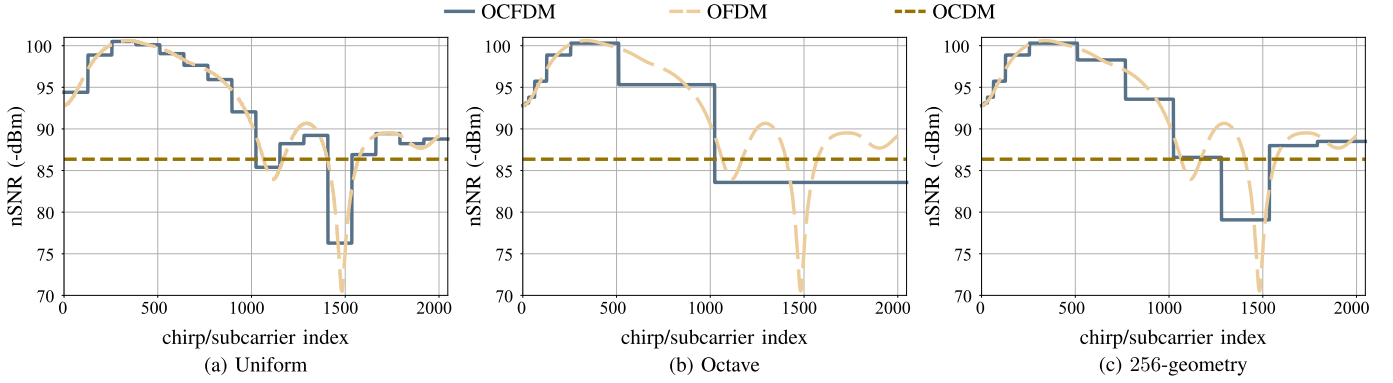


Fig. 5. nSNR comparison among the OFDM, OCDM, and OCFDM: (a) Uniform, (b) Octave, and (c) 256-geometry; for one channel realization.

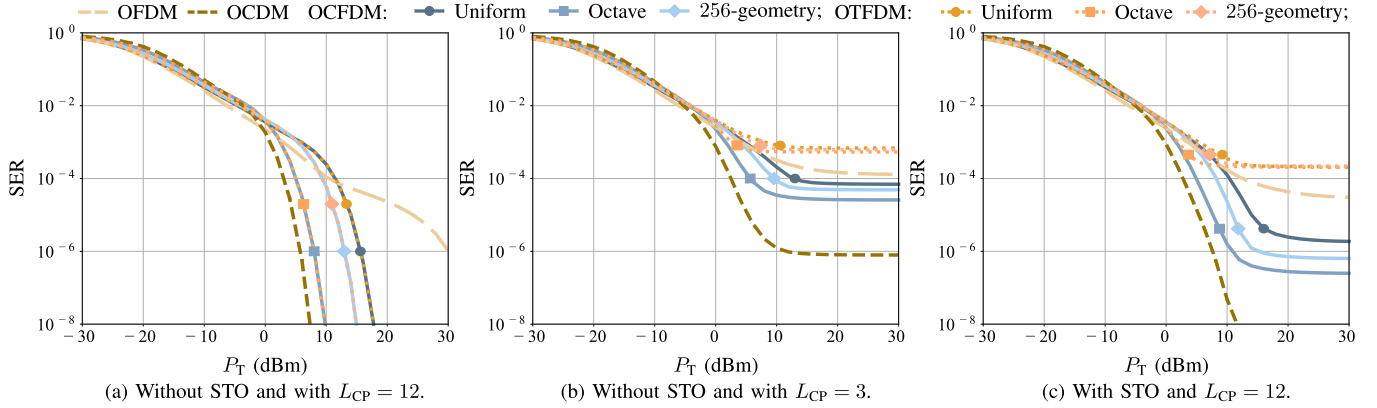


Fig. 6. $SER \times P_T$ for the OCFDM, OFDM, OCDM, and OTFDM with uncoded 16-QAM constellation: ISI is produced by STO and CP length violation.

This variation of the nSNR from one voice to another opens the possibility of implementing resource allocation techniques. Also, since the nSNR of the OCFDM follows the voices and not the chirps, it brings an advantage over the OFDM regarding the feedback of the CSI to the transmitter. Whereas the OFDM needs to send the information of N subcarriers, the OCFDM only needs to send information of N_p voices. In our numerical example, the OFDM receiver fed back nSNRs of 2048 different subcarriers, while the OCFDM receiver only fed back nSNRs of 12 or 16 voices. Note that the subcarrier chunking into voices is also performed by the OTFDM technique since it uses the geometries adopted by the OCFDM.

The geometries presented in Table III will be considered henceforth.

B. SER Related to STO and CP Length Violation

For the SER performance analysis, uniform allocation of $P_T \in [-30, 30]$ dBm and uncoded 16-QAM constellation were adopted in all techniques. It was also considered three different scenarios of ISI. The first one means that the all techniques operated without the ISI induced by STO (*i.e.*, perfect symbol synchronization) and assumed CP length was correct (*i.e.*, $L_{CP} \geq L_h - 1$); the second means all techniques operated without ISI due to STO (*i.e.*, perfect symbol synchronization) and assumed the violation of the CP length (*i.e.*, $L_{CP} \geq L_h - 1$); and the third means all techniques operated under the presence of STO equivalent to one sample (*i.e.*, imperfect symbol

synchronization) and correct CP length (*i.e.*, $L_{CP} < L_h - 1$). The formulation employed to obtain the SER under these types of ISI can be found in [38].

Fig. 6 depicts the curves of $SER \times P_T$ comparing the OCFDM with OCDM, OFDM, and OTFDM. We can see that, for higher values of P_T , the OCDM yielded the best values of SER and the OFDM yielded the worst ones. For all scenarios, the SER of the OCFDM, considering all geometries, behaved according to the following pattern: the Octave tile geometry presented a performance closer to the OCDM, the Uniform tile geometry performed closer to the OFDM, and the 256-geometry was in between the Uniform and Octave geometries. For instance, Fig. 6(a) shows that to achieve a SER close to 10^{-6} , transmission power of 5, 8, 13, 15, and 30 dBm was required when adopting the OCDM, Octave OCFDM, 256-geometry OCFDM, Uniform OCFDM, and OFDM, respectively, when STO and CP length violation are absent. Furthermore, the geometries reacted differently to the presence of ISI; for instance, geometries such as the Uniform and 256-geometry suffered more with ISI than the Octave; see Fig. 6(b)-(c). When looking at the case without STO and with $L_{CP} = 3$, only the OCDM reached a SER of 10^{-6} , whereas the OCFDM yielded a minimum SER of 2.60×10^{-5} , 4.88×10^{-5} , and 6.96×10^{-5} , for the Octave, Uniform, and 256-geometry, respectively, and the OFDM a minimum SER of 1.2×10^{-4} . Another example reinforcing this comparison is depicted in Fig. 6(c), where it is clear the advantage of using chirps to deal with ISI due to STO. The OFDM, in this case,

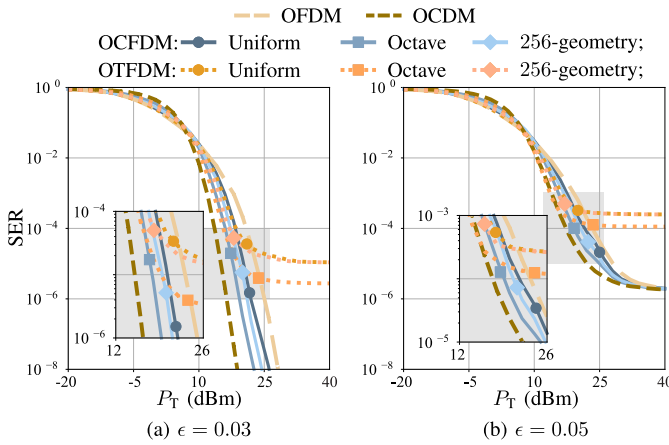


Fig. 7. SER \times P_T for the OCFDM, OFDM, OCDM, and OTFDM with uncoded 16-QAM constellation: The interference caused by a normalized CFO of (a) $\epsilon = 0.03$ and (b) $\epsilon = 0.05$.

yielded a minimum SER of 3.05×10^{-5} with $P_T = 30$ dBm, while the OCFDM with Uniform, 256-geometry, and Octave yielded minimum SER of 1.86×10^{-6} , 6.37×10^{-7} , and 2.49×10^{-7} , respectively. This assessment of the OCFDM performance shows the flexibility that comes from choosing a tile geometry, meaning that different geometries lead to different SER performances and robustness to interference.

Furthermore, a comparison between the OCFDM and OTFDM is appropriate for both since they possess the same nSNR [24]. Indeed, the OTFDM also uses a time-frequency transform governed by β , ν , and τ to process the modulated signals digitally. For the case without ISI, both techniques attained the same performance for each tile geometry. However, the presence of ISI extremely degraded the performance of the OTFDM in comparison to the OCFDM. For instance, in Fig. 6(b)-(c), which characterize the scenario with interference, the SERs achieved by the OTFDM were bigger than 10^{-4} for all geometries considered. On the other hand, the OCFDM achieved a SER lower than 10^{-4} , with all geometries, for the case depicted in Fig. 6(b) and close to 1.86×10^{-6} , 6.37×10^{-7} , and 2.49×10^{-7} for the Uniform, 256-geometry, and Octave, respectively, for the case in Fig. 6(c).

C. SER Related to CFO

This section analyzes the CFO influence in the SER performance. In this sense, the simulations carried out rely on the model for CFO presented in [39] and [40] and adapted to the OCFDM and OTFDM. The theoretical development for the OCFDM technique disturbed by CFO is detailed in Appendix A. Moreover, our analysis considered two different levels of CFO intensity. All other considerations were the same ones presented in the analysis under the perfect conditions detailed in Section V-B.

Fig. 7(a) shows the SER \times P_T curves for the data communication system operating under normalized CFO of $\epsilon = 0.03$, while Fig. 7(b) shows the curves for $\epsilon = 0.05$. The SER curves with CFO of all techniques were computed for $P_T \in [-20, 40]$ dBm. These plots reveal that the interference caused by CFO yielded SER results similar to those showed

in Fig. 6(b)-(c) for all techniques considered. That is, OCDM exhibited the best robustness to interference, followed by OCFDM and OFDM, while OTFDM still attained the worst performance. As an example, considering $\epsilon = 0.03$, to yield a SER of 10^{-6} , the OCDM required a P_T of 16 dBm, the OCFDM required 22, 21, and 19 dBm for the OCFDM with Uniform, 256-geometry, and Octave, respectively, and 27 dBm for the OFDM. On the other hand, the OTFDM lowest value of SER was around 2.82×10^{-6} with Octave geometry.

With the increase in interference, i.e., adopting $\epsilon = 0.05$, the performance of all techniques was heavily degraded. For high values of P_T , the SER performances of the OCFDM, the OCDM, and the OFDM converged to 1.84×10^{-6} while the OTFDM yielded next to 1.12×10^{-4} with Octave tile geometry and 2.49×10^{-4} for the other geometries.

D. BER for Uncoded and Coded Techniques

This section presents the numerical results regarding the use of forward error correction (FEC) in OFDM, OCDM, OTFDM, and OCFDM techniques. In this sense, we considered convolutional code with a code rate of 1/2 and a constraint length of 7 bits [41]. We also considered LDPC [42] codes with a codeword length of 8192 bits with code rates of 1/4, 1/2, and 3/4 and 20 iterations. Moreover, 4-QAM constellation, minimum mean squared error equalization, and log-likelihood ratio demodulation were adopted. The analyses were carried out in terms of BER \times E_b/N_0 (dB) for comparing uncoded and coded transmissions.

Regarding the use of the convolutional coding, Fig. 8 shows the BER \times E_b/N_0 curves for the coded and uncoded OFDM, OCDM, OCFDM, and OTFDM techniques. The numerical results show that using convolutional codes improved the BER of all techniques. Indeed, all coded techniques using convolutional code required approximately less 3 dB to attain a BER of 10^{-5} compared to the uncoded ones. Furthermore, the relative performance improvement offered by convolutional code was analogous to the uncoded ones, in the sense that the OCDM presented the best results of BER in medium to higher values of E_b/N_0 , being followed by the OCFDM with Octave, 256-geometry, Uniform, and OFDM. Moreover, the coded OTFDM performed equal to the coded OCFDM.

Considering the use of LDPC coding, the curves of BER \times E_b/N_0 for the coded and uncoded OFDM, OCDM, OCFDM, and OTFDM techniques are shown in Fig. 9. The BER values obtained show much improvement to the OFDM's performance when the coded and uncoded techniques are compared,⁸ making it akin to the ones obtained by the OCFDM with code rates of 1/2 and 1/4. Indeed, the BER achieved by the OFDM and the OCFDM, considering all geometries, were similar for all values of E_b/N_0 with a code rate of 1/2 and even performing slightly better than the OCDM for a code rate of 1/4. Furthermore, for the OCFDM, the performance between its geometries was preserved because the Octave performed better, followed by the 256-geometry and Uniform; however, the difference between them was tiny. For code rates of 1/2 and 3/4, the OCDM attained the best performance.

⁸To see this, one needs to compare the curves in Fig. 8(b) and Fig. 9.

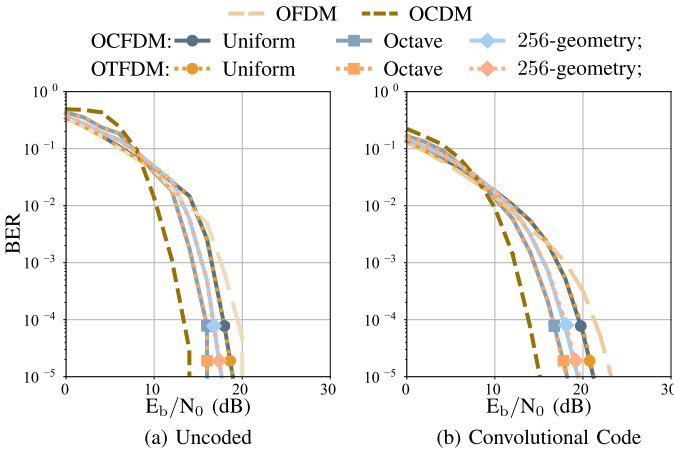


Fig. 8. BER $\times E_b/N_0$ for the OCFDM, OFDM, OCDM, and OTFDM with 4-QAM constellation: (a) convolutional code, (b) unencoded.

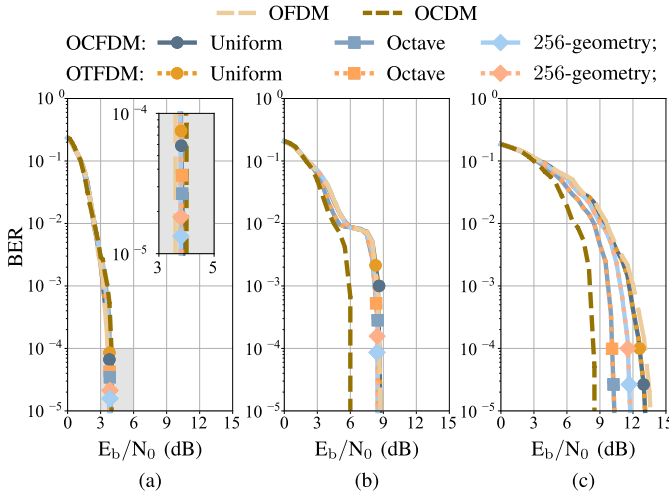


Fig. 9. BER $\times E_b/N_0$ for the OCFDM, OFDM, OCDM, and OTFDM with 4-QAM constellation and LDPC code with code rates of (a) 1/4, (b) 1/2, and (c) 3/4.

For instance, the OCDM attained a BER of 10^{-5} requiring on average 3 dB less E_b/N_0 than the other techniques with a code rate of 1/2. Finally, the OTFDM technique achieved the same performance of the OCFDM, for every geometry and code rate.

E. Data Rate Comparison

The data rate analysis was performed considering the scenarios of uniform power allocation (UA) and water-filling power allocation (WFA), while considering an uncoded modulator. We considered $\Gamma = 9.25$ dB for all allocation cases, which imposes a SER fixed at 10^{-6} for QAM modulation [21]. As the OFDM attained the highest data rates, we computed and analyzed data rate values normalized by the OFDM ones, which are denoted by \bar{R} , with UA and WFA. It is important to mention that we omitted the computed data rates of OFDM since it is implied in Fig. 10(a) and of OTFDM because it is equal to those obtained by OCFDM.⁹

⁹Using the same tile geometry, OTFDM and OCFDM offer the same nSNR and, consequently, equal data rates.

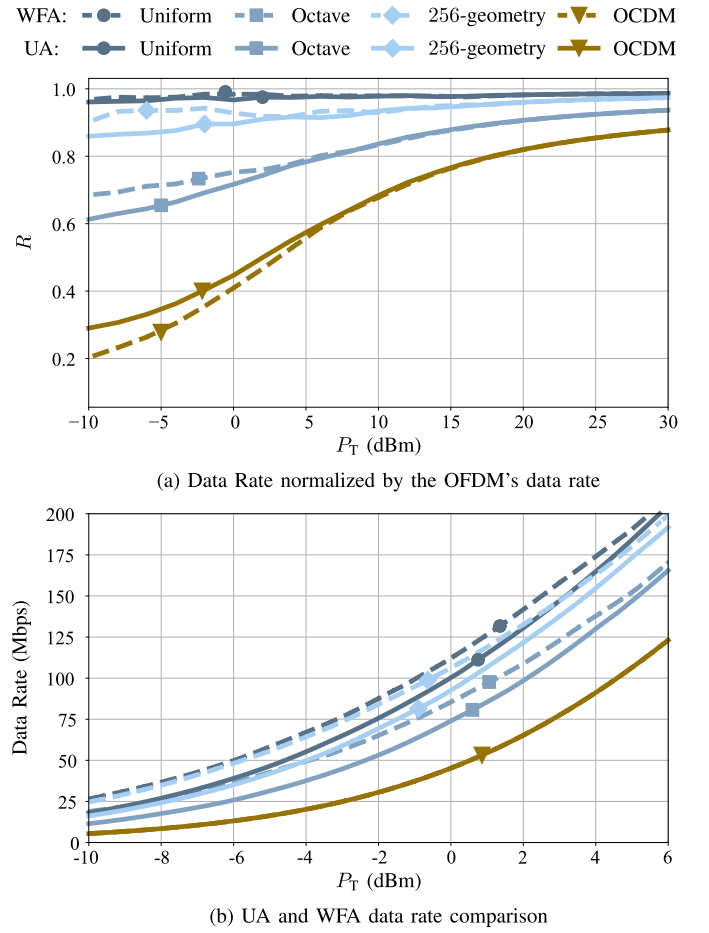


Fig. 10. (a) $\bar{R} \times P_T$ and (b) $R \times P_T$ considering UA (solid lines) and WFA (dashed lines).

Fig. 10(a) shows the curves of normalized data rates when the transmission power is allocated using UA and WFA for $P_T \in [-10, 30]$ dBm. Note that the OFDM attained the highest data rates for all values of P_T and allocation techniques, which is confirmed since none of its curves presented $\bar{R} \geq 1$. Inversely, the OCDM data rate was the lowest, yielding the same result when using UA and WFA, as expected from the remarks of Section IV-B. The OCFDM performance was very close to the one yielded by the OFDM. With UA, the Uniform tile geometry went from $\bar{R} = 0.95$ to $\bar{R} = 0.99$, with the increase of P_T . Furthermore, with slightly lower performance than the Uniform tile geometry, the 256-geometry normalized data rate varied from $\bar{R} = 0.87$ to $\bar{R} = 0.97$ and the Octave tile geometry, which presented the worst performance among all three geometries, increased from $\bar{R} = 0.64$ to $\bar{R} = 0.94$. Regarding the use of WFA, it is noticeable that the water-filling algorithm improved the data rate of all three geometries for low values of P_T , as it is shown in Fig. 10(b). For instance, with $P_T = 0$ dBm, the Uniform, Octave, and 256-geometry respectively yielded 100.27, 74.00, and 92.55 Mbps with UA, and 112.15, 85.42, and 111.79 Mbps with WFA.

F. PAPR Comparison

This section details a comparison in terms of PAPR between OCFDM, OFDM, OCDM, and OTFDM. To this end, numer-

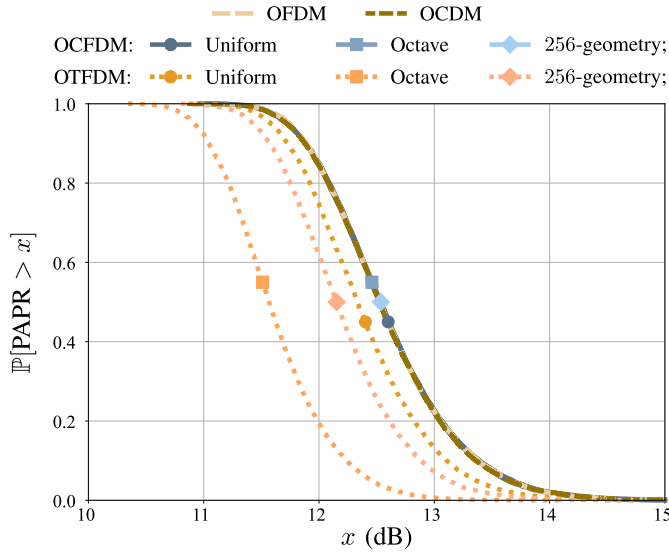


Fig. 11. PAPR results for the OCFDM, OFDM, OCDM, and OTFDM.

ical simulations were carried out following the parameters defined at the beginning of Section V while considering the N chirps/subcarriers/tiles being modulated with equiprobable uncoded symbols belonging to the 16-QAM constellation with an oversampling factor of 4 and the addition of 3 dB to emulate an accurate passband modulation PAPR [43], [44].

Fig. 11 shows the complementary cumulative distribution function (CCDF) of the PAPR for all techniques. The PAPR for the OCDM and OFDM have already been studied in other papers [3], [6], [43], and they presented the same behavior in our numerical simulations. The OCFDM followed this behavior regardless of the chosen tile geometry, meaning that all three techniques mentioned earlier possess the same CCDF for the PAPR. Furthermore, we can state that the tile geometry does not alter the PAPR by itself for the OCFDM.

On the other hand, the OTFDM yielded different PAPR curves for each tile geometry, with the Octave performing better, followed by the 256-geometry and the Uniform, and all presenting a better PAPR than the other three techniques.

VI. CONCLUSION

This paper detailed the OCFDM, a novel data communication technique that uses the DMCT as the core operation. DMCT creates divisions in the frequency band and fill them with orthogonal chirps, thus yielding a CSS-based technique featuring flexibility.

Numerical simulations were carried out to analyze: nSNR through the frequency band; SER under the presence of STO, CP length violation and CFO; BER for the uncoded and coded techniques; data rate with and without resource allocation; and PAPR while using the OFDM, OCDM, and OTFDM as benchmarks. The OCFDM yields an nSNR that varies with the voice, allowing the use of resource allocation algorithms. Also, compared to the OFDM, it requires less feedback information because the number of voices is significantly reduced compared to the number of subcarriers. Furthermore, we verified that the OCFDM performs in-between the OFDM and OCDM

in terms of SER and data rate. Also, the choice of its tile geometry is an added degree of freedom that may favor aspects more related to OFDM or OCDM and, consequently, create interesting trade-offs in terms of SER, data rate, and robustness to deal with different types of interference. Moreover, the OCFDM outperformed the OTFDM in terms of SER when facing interference originating from CP length violation, STO, and CFO, but it presented a worse PAPR performance (akin to the OFDM's).

APPENDIX A CFO IN OCFDM

The CFO is defined as the difference in frequency between the oscillators of the transmitter and the receiver. This frequency mismatch is denoted by $\Delta_f = f_{TX} - f_{RX}$, where f_{TX} is the frequency of the transmitter oscillator and f_{RX} is the frequency of the receiver oscillator. To analyze the OCFDM in the presence of CFO, it is necessary to redefine the i^{th} received OCFDM block, obtained after the removal of CP, with the inclusion of the CFO distortion as follows [39], [40]:

$$\mathbf{y}^{(i)} = e^{j\frac{2\pi\epsilon(i\tilde{N}+L_{CP})}{N}} \mathbf{\Lambda}_{CFO} \mathbf{C}_h \mathbf{x}^{(i)} + \mathbf{v}, \quad (55)$$

wherein $\tilde{N} = N + L_{CP}$, $\epsilon = \Delta_f N T_s$ is the normalized CFO, with T_s being the sampling period, and $\mathbf{\Lambda}_{CFO}$ is a diagonal matrix with elements equal to $\Lambda_{CFO,n,n} = \exp(j2\pi\epsilon n/N)$, $n \in [0, N-1]$. Following the OCFDM reception, the i^{th} received OCFDM block is processed by the DMCT transform, resulting in the i^{th} estimated block symbol given by

$$\begin{aligned} \hat{\mathbf{x}}_M^{(i)} &= e^{j\frac{2\pi\epsilon(i\tilde{N}+L_{CP})}{N}} \overline{\mathbf{M}} \mathbf{E} \mathbf{F}_N \mathbf{\Lambda}_{CFO} \mathbf{C}_h \mathbf{F}_N^\dagger \overline{\mathbf{M}}^\dagger \mathbf{x}_M^{(i)} + \overline{\mathbf{M}} \mathbf{E} \mathbf{F}_N \mathbf{v} \\ &= e^{j\frac{2\pi\epsilon(i\tilde{N}+L_{CP})}{N}} \overline{\mathbf{M}} \mathbf{E} \mathbf{F}_N \mathbf{\Lambda}_{CFO} \mathbf{F}_N^\dagger \mathbf{F}_N \mathbf{C}_h \mathbf{F}_N^\dagger \overline{\mathbf{M}}^\dagger \mathbf{x}_M^{(i)} + \overline{\mathbf{M}} \mathbf{E} \mathbf{v}_F \\ &= e^{j\frac{2\pi\epsilon(i\tilde{N}+L_{CP})}{N}} e^{j\frac{\pi\epsilon(N-1)}{N}} \overline{\mathbf{M}} \mathbf{E} \mathbf{C}_{CFO} \mathbf{\Lambda}_{h_F} \overline{\mathbf{M}}^\dagger \mathbf{x}_M^{(i)} + \overline{\mathbf{M}} \mathbf{E} \mathbf{v}_F, \end{aligned} \quad (56)$$

in which $\mathbf{F}_N \mathbf{\Lambda}_{CFO} \mathbf{F}_N^\dagger = \exp(j\pi\epsilon(N-1)/N) \mathbf{C}_{CFO}$, with \mathbf{C}_{CFO} being a circulant matrix with the element of the m^{th} row and n^{th} column given by

$$C_{CFO,m,n} = \frac{\sin[\pi(\epsilon + \text{mod}(n-m, N))]}{N \sin[\frac{\pi}{N}(\epsilon + \text{mod}(n-m, N))]} \times e^{j\frac{\pi(N-1)}{N} \text{mod}(n-m, N)}, \quad (57)$$

in which $c = \text{mod}(a, b)$ with $a, b, c \in \mathbb{Z}$ returns the rest of a divided by b . We consider a scenario in which the receiver accurately performs channel estimation, allowing the equalizer, \mathbf{E} , to eliminate the phase-shift term common to all chirps and blocks, i.e., $\exp(j\pi\epsilon(N-1)/N)$ and $\exp(j2\pi\epsilon(i\tilde{N}+L_{CP})/N)$, respectively. Therefore, when applying a ZF equalization, the equalizer of the i^{th} block is given by $\mathbf{E} = \exp(-j2\pi\epsilon(i\tilde{N}+L_{CP})/N) \exp(-j\pi\epsilon(N-1)/N) \mathbf{\Lambda}_{h_F}^{-1}$. Consequently, analyzing the estimated signal by its block index is unnecessary, leading to a time-invariant scenario. Even though part of the CFO was mitigated by the equalizer,

some interference remains in the form of the matrix \mathbf{C}_{CFO} . Thus, the reconstructed estimated block symbol is reduced to

$$\hat{\mathbf{x}}_{\text{M}} = \bar{\mathbf{M}}\mathbf{\Lambda}_{\text{HF}}^{-1}\mathbf{C}_{\text{CFO}}\mathbf{\Lambda}_{\text{HF}}\bar{\mathbf{M}}^{\dagger}\mathbf{x}_{\text{M}} + \bar{\mathbf{M}}\mathbf{\Lambda}_{\text{HF}}^{-1}\mathbf{v}_{\text{F}}. \quad (58)$$

This equation shows that the distortions caused by the CFO break the orthogonality of the OCFDM technique, creating interference between the transmitted symbols.

Now, taking a closer look at the estimated symbol related to the p^{th} voice, we have

$$\begin{aligned} \hat{\mathbf{x}}_{\text{M}_p} = & \bar{\mathbf{M}}_p\mathbf{\Lambda}_{\text{HF},p}^{-1}\mathbf{C}_{\text{CFO},p,p}\mathbf{\Lambda}_{\text{HF},p}\bar{\mathbf{M}}_p^{\dagger}\mathbf{x}_{\text{M}_p} + \sum_{\substack{k=0 \\ k \neq p}}^{N_p-1} \bar{\mathbf{M}}_p\mathbf{\Lambda}_{\text{HF},p}^{-1} \\ & \times \mathbf{C}_{\text{CFO},p,k}\mathbf{\Lambda}_{\text{HF},k}\bar{\mathbf{M}}_k^{\dagger}\mathbf{x}_{\text{M}_k} + \bar{\mathbf{M}}_p\mathbf{\Lambda}_{\text{HF},p}^{-1}\mathbf{v}_{\text{F}_p}, \end{aligned} \quad (59)$$

wherein the element of the a^{th} row and b^{th} column of the matrix $\mathbf{C}_{\text{CFO},p,k} \in \mathbb{C}^{\beta_p \times \beta_k}$ is equal to $C_{\text{CFO},\text{lb}_p+a,\text{lb}_k+b}$ with $a \in [0, \beta_p - 1]$ and $b \in [0, \beta_k - 1]$. From (59), we can identify which terms represent the desired chirps, interchirp interference (ICpI), and noise. To this end, we define the matrix $\mathcal{D}\{\mathbf{A}\}$ as a diagonal matrix with elements equal to the main diagonal of \mathbf{A} , $\widetilde{\mathbf{M}}_{p,k} = \bar{\mathbf{M}}_p\mathbf{\Lambda}_{\text{HF},p}^{-1}\mathbf{C}_{\text{CFO},p,k}\mathbf{\Lambda}_{\text{HF},k}\bar{\mathbf{M}}_k^{\dagger}$, and rewrite (59) as

$$\begin{aligned} \hat{\mathbf{x}}_{\text{M}_p} = & \underbrace{\mathcal{D}\{\widetilde{\mathbf{M}}_{p,p}\}\mathbf{x}_{\text{M}_p}}_{\text{desired chirps}} + \underbrace{\left(\widetilde{\mathbf{M}}_{p,p} - \mathcal{D}\{\widetilde{\mathbf{M}}_{p,p}\}\right)\mathbf{x}_{\text{M}_p}}_{\text{ICpI from the } p^{\text{th}} \text{ voice}} \\ & + \underbrace{\sum_{\substack{k=0 \\ k \neq p}}^{N_p-1} \widetilde{\mathbf{M}}_{p,k}\mathbf{x}_{\text{M}_k}}_{\text{ICpI from the } k^{\text{th}} \text{ voice}} + \underbrace{\bar{\mathbf{M}}_p\mathbf{\Lambda}_{\text{HF},p}^{-1}\mathbf{v}_{\text{F}_p}}_{\text{noise}}. \end{aligned} \quad (60)$$

A. SINR Calculation

This section discusses the signal-to-interference-plus-noise ratio (SINR) of the OCFDM technique operating under CFO. When considering the modulated signal and noise as random vectors, we interpret the estimated signal related to the p^{th} voice, $\hat{\mathbf{x}}_{\text{M}_p}$, as a vector containing realizations of the random variable $\hat{\mathcal{X}}_{\text{M}_p,m}$ and given by

$$\begin{aligned} \hat{\mathcal{X}}_{\text{M}_p} = & \underbrace{\mathcal{D}\{\widetilde{\mathbf{M}}_{p,p}\}\mathcal{X}_{\text{M}_p}}_{\text{desired chirps}} + \underbrace{\left(\widetilde{\mathbf{M}}_{p,p} - \mathcal{D}\{\widetilde{\mathbf{M}}_{p,p}\}\right)\mathcal{X}_{\text{M}_p}}_{\text{ICpI from the } p^{\text{th}} \text{ voice}} \\ & + \underbrace{\sum_{\substack{k=0 \\ k \neq p}}^{N_p-1} \widetilde{\mathbf{M}}_{p,k}\mathcal{X}_{\text{M}_k}}_{\text{ICpI from the other voices}} + \underbrace{\bar{\mathbf{M}}_p\mathbf{\Lambda}_{\text{HF},p}^{-1}\mathbf{v}_{\text{F}_p}}_{\text{noise}}, \end{aligned} \quad (61)$$

in which \mathcal{X}_{M_p} and \mathbf{v}_{F_p} are $\beta_p \times 1$ random vectors whose components' realizations are $x_{\text{M}_p,m}$ and $v_{\text{F}_p,k}$, respectively. Moreover, chirps from the same voice are transmitted with equal power such that the power associated with the chirps of the p^{th} voice can be extracted from the main diagonal of the matrix:

$$\begin{aligned} \mathbf{P}_{\text{X}_{\text{M}_p}} &= \mathbb{E}\{\mathcal{X}_{\text{M}_p}\mathcal{X}_{\text{M}_p}^{\dagger}\} \\ &= P_{\text{X}_{\text{M}_p,m}}\mathbf{I}_{\beta_p}, \end{aligned} \quad (62)$$

in which the power allocated to a voice, $\beta_p P_{\text{X}_{\text{M}_p,m}}$, is determined by a factor ρ_p with $0 \leq \rho_p \leq 1$ and $\sum_{p=0}^{N_p} \rho_p = 1$, making $P_{\text{X}_{\text{M}_p,m}} = \rho_p P_{\text{T}}/\beta_p$ and the sum of power allocated to each voice being equal to the total transmission power, or $P_{\text{T}} = \sum_{p=0}^{N_p-1} \beta_p P_{\text{X}_{\text{M}_p,m}}$. The power associated with the vector containing the noise realizations at the p^{th} voice can be extracted from the main diagonal of the following matrix:

$$\begin{aligned} \mathbf{P}_{\text{V}_p} &= \mathbb{E}\{\mathbf{v}_{\text{F}_p}\mathbf{v}_{\text{F}_p}^{\dagger}\} \\ &= P_{\text{V}_p}\mathbf{I}_{\beta_p}. \end{aligned} \quad (63)$$

Consequently, the SINR vector associated with the p^{th} voice is given by the diagonal elements of the following matrix:

$$\begin{aligned} \mathbf{\Lambda}_{\gamma_p} = & \frac{\rho_p}{\beta_p} P_{\text{T}}\mathbf{\Lambda}_{\text{des},p} \left(\frac{\rho_p}{\beta_p} P_{\text{T}}\mathbf{\Lambda}_{\text{ICpI},p} \right. \\ & \left. + \sum_{\substack{k=0 \\ k \neq p}}^{N_p-1} \frac{\rho_k}{\beta_k} P_{\text{T}}\mathbf{\Lambda}_{\text{ICpI},p,k} + P_{\text{V}_p}\mathbf{\Lambda}_{\text{V}_p} \right)^{-1}, \end{aligned} \quad (64)$$

in which

$$\mathbf{\Lambda}_{\text{des},p} = \mathcal{D}\{\widetilde{\mathbf{M}}_{p,p}\}\mathcal{D}\{\widetilde{\mathbf{M}}_{p,p}\}^{\dagger}, \quad (65)$$

$$\begin{aligned} \mathbf{\Lambda}_{\text{ICpI},p} = & \mathcal{D}\left\{\left(\widetilde{\mathbf{M}}_{p,p} - \mathcal{D}\{\widetilde{\mathbf{M}}_{p,p}\}\right) \right. \\ & \left. \times \left(\widetilde{\mathbf{M}}_{p,p} - \mathcal{D}\{\widetilde{\mathbf{M}}_{p,p}\}\right)^{\dagger}\right\}, \end{aligned} \quad (66)$$

$$\mathbf{\Lambda}_{\text{ICpI},p,k} = \mathcal{D}\left\{\widetilde{\mathbf{M}}_{p,k}\widetilde{\mathbf{M}}_{p,k}^{\dagger}\right\}, \quad (67)$$

and

$$\mathbf{\Lambda}_{\text{V}_p} = \mathcal{D}\left\{\bar{\mathbf{M}}_p\mathbf{\Lambda}_{\text{HF},p}^{-1}\mathbf{\Lambda}_{\text{HF},p}^{-1*}\bar{\mathbf{M}}_p^{\dagger}\right\}. \quad (68)$$

Finally, we can derive an upper bound for the SINR by infinitely increasing the value of P_{T} . Therefore, we define

$$\begin{aligned} \dot{\mathbf{\Lambda}}_{\gamma_p} &\triangleq \lim_{P_{\text{T}} \rightarrow \infty} \mathbf{\Lambda}_{\gamma_p} \\ &= \frac{\rho_p}{\beta_p} \mathbf{\Lambda}_{\text{des},p} \left(\frac{\rho_p}{\beta_p} \mathbf{\Lambda}_{\text{ICpI},p} + \sum_{\substack{k=0 \\ k \neq p}}^{N_p-1} \frac{\rho_k}{\beta_k} \mathbf{\Lambda}_{\text{ICpI},p,k} \right)^{-1}, \end{aligned} \quad (69)$$

as the diagonal matrix containing the upper bound SINR values related to the p^{th} voice. Thus, any monotonic continuous function of the SINR, including the figures of merit considered in this work, will present saturation as P_{T} grows to infinity. For instance, SER of systems operating with the presence of CFO will present a lower bound due to (69).

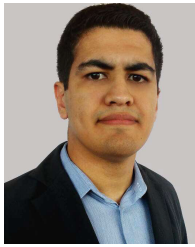
REFERENCES

- [1] P. S. R. Diniz, W. A. Martins, and M. V. S. Lima, *Block Transceivers: OFDM and Beyond*. San Rafael, CA, USA: Morgan & Claypool, 2012.
- [2] G. Cuoizzo, N. Longhi, and G. Pasolini, "Characterization of orthogonal chirp division multiplexing and performance evaluation at THz frequencies in the presence of phase noise," *IEEE Open J. Commun. Soc.*, vol. 5, pp. 238–255, 2024, doi: [10.1109/OJCOMS.2023.3340091](https://doi.org/10.1109/OJCOMS.2023.3340091).
- [3] L. de M. B. A. Dib, G. R. Colen, M. de L. Filomeno, and M. V. Ribeiro, "Orthogonal chirp division multiplexing for baseband data communication systems," *IEEE Syst. J.*, vol. 14, no. 2, pp. 2164–2174, Jun. 2020.

- [4] M. de L. Filomeno, T. F. Moreira, Y. F. Coutinho, Â. Camponogara, M. L. R. de Campos, and M. V. Ribeiro, "Orthogonal chirp-division multiplexing-based hybrid power line/wireless system," in *Proc. IEEE Global Commun. Conf. (GLOBECOM)*, Rio de Janeiro, Brazil, Dec. 2022, pp. 5880–5885.
- [5] B. Wang, Y. Wang, Y. Li, and X. Guan, "Underwater acoustic communications based on OCDM for Internet of underwater things," *IEEE Internet Things J.*, vol. 10, no. 24, pp. 22128–22142, Dec. 2023.
- [6] X. Ouyang and J. Zhao, "Orthogonal chirp division multiplexing," *IEEE Trans. Commun.*, vol. 64, no. 9, pp. 3946–3957, Sep. 2016.
- [7] R. Bomfin, M. Chafii, and G. Fettweis, "Performance assessment of orthogonal chirp division multiplexing in MIMO space time coding," in *Proc. IEEE 2nd 5G World Forum (5GWF)*, Dresden, Germany, Sep. 2019, pp. 220–225.
- [8] M. S. Omar and X. Ma, "Performance analysis of OCDM for wireless communications," *IEEE Trans. Wireless Commun.*, vol. 20, no. 7, pp. 4032–4043, Jul. 2021.
- [9] X. Ouyang, O. A. Dobre, and J. Zhao, "Unbiased channel estimation based on the discrete Fresnel transform for CO-OFDM systems," *IEEE Photon. Technol. Lett.*, vol. 29, no. 8, pp. 691–694, Apr. 15, 2017.
- [10] X. Ouyang, C. Antony, G. Talli, and P. D. Townsend, "Robust channel estimation for coherent optical orthogonal chirp-division multiplexing with pulse compression and noise rejection," *J. Lightw. Technol.*, vol. 36, no. 23, pp. 5600–5610, Dec. 1, 2018.
- [11] M. de L. Filomeno et al., "Joint channel estimation and Schmidl & Cox synchronization for OCDM-based systems," *IEEE Commun. Lett.*, vol. 26, no. 8, pp. 1878–1882, Aug. 2022.
- [12] L. Giroto de Oliveira, M. B. Alabd, B. Nuss, and T. Zwick, "An OCDM radar-communication system," in *Proc. 14th Eur. Conf. Antennas Propag. (EuCAP)*, Copenhagen, Denmark, Mar. 2020, pp. 1–5.
- [13] L. Giroto de Oliveira, B. Nuss, M. B. Alabd, Y. Li, L. Yu, and T. Zwick, "MIMO-OCDM-based joint radar sensing and communication," in *Proc. 15th Eur. Conf. Antennas Propag. (EuCAP)*, Dusseldorf, Germany, Mar. 2021, pp. 1–5.
- [14] L. Giroto de Oliveira, B. Nuss, M. B. Alabd, A. Diewald, M. Pauli, and T. Zwick, "Joint radar-communication systems: Modulation schemes and system design," *IEEE Trans. Microw. Theory Techn.*, vol. 70, no. 3, pp. 1521–1551, Mar. 2022.
- [15] L. Giroto de Oliveira, M. de L. Filomeno, H. V. Poor, and M. V. Ribeiro, "Orthogonal chirp-division multiplexing for power line sensing via time-domain reflectometry," *IEEE Sensors J.*, vol. 21, no. 2, pp. 955–964, Jan. 2021.
- [16] P.-J. Bouvet, Y. Auffret, and C. Aubry, "On the analysis of orthogonal chirp division multiplexing for shallow water underwater acoustic communication," in *Proc. OCEANS*, Aberdeen, U.K., Jun. 2017, pp. 1–5.
- [17] P. Zhu, X. Xu, X. Tu, Y. Chen, and Y. Tao, "Anti-multipath orthogonal chirp division multiplexing for underwater acoustic communication," *IEEE Access*, vol. 8, pp. 13305–13314, 2020.
- [18] A. Bemani, N. Ksairi, and M. Kountouris, "Affine frequency division multiplexing for next generation wireless communications," *IEEE Trans. Wireless Commun.*, vol. 22, no. 11, pp. 8214–8229, Nov. 2023.
- [19] R. Hadani et al., "Orthogonal time frequency space modulation," in *Proc. IEEE Wireless Commun. Netw. Conf. (WCNC)*, San Francisco, CA, USA, Mar. 2017, pp. 1–6.
- [20] T. F. Moreira, Â. Camponogara, S. Baig, and M. V. Ribeiro, "Data rate and bit error probability in narrowband PLC systems: OCDM versus HS-OFDM," in *Proc. 39th Simpósio Brasileiro de Telecomunicações e Processamento de Sinais (SBrT)*, Fortaleza, Brazil, Sep. 2021, pp. 1–5.
- [21] L. Giroto de Oliveira, G. R. Colen, A. H. Vinck, and M. V. Ribeiro, "Resource allocation in HS-OFDM-based PLC systems: A tutorial," *J. Commun. Inf. Syst.*, vol. 33, pp. 308–321, Oct. 2018.
- [22] M. S. Omar and X. Ma, "Designing OCDM-based multi-user transmissions," in *Proc. IEEE Global Commun. Conf. (GLOBECOM)*, Waikoloa, HI, USA, Dec. 2019, pp. 1–6.
- [23] R. G. Stockwell, "A basis for efficient representation of the S-transform," *Digit. Signal Process.*, vol. 17, no. 1, pp. 371–393, Jan. 2007.
- [24] G. R. Colen and M. V. Ribeiro, "A flexible multicarrier scheme based on the discrete orthogonal Stockwell transform," *IEEE Syst. J.*, vol. 14, no. 4, pp. 5284–5295, Dec. 2020.
- [25] T. F. Moreira, M. de L. Filomeno, W. A. Martins, and M. V. Ribeiro, "A frequency division modulation for CSS-based communication systems: An initial discussion," in *Proc. Symp. Internet Things (SIoT)*, São Paulo, Brazil, Oct. 2023, pp. 1–5.
- [26] C. Beuter and M. Oleskovicz, "S-transform: From main concepts to some power quality applications," *IET Signal Process.*, vol. 14, no. 3, pp. 115–123, May 2020.
- [27] C. Herley, J. Kovacevic, K. Ramchandran, and M. Vetterli, "Tilings of the time-frequency plane: Construction of arbitrary orthogonal bases and fast tiling algorithms," *IEEE Trans. Signal Process.*, vol. 41, no. 12, pp. 3341–3359, Dec. 1993.
- [28] I. Daubechies, "The wavelet transform, time-frequency localization and signal analysis," *IEEE Trans. Inf. Theory*, vol. 36, no. 5, pp. 961–1005, Sep. 1990.
- [29] Y.-P. Lin and S.-M. Phoong, "BER minimized OFDM systems with channel independent precoders," *IEEE Trans. Signal Process.*, vol. 51, no. 9, pp. 2369–2380, Sep. 2003.
- [30] P. S. Bullen, *Handbook of Means and Their Inequalities*. Dordrecht, The Netherlands: Springer, 2003.
- [31] T. M. Cover and J. A. Thomas, *Elements of Information Theory*, 2nd ed., Hoboken, NJ, USA: Wiley, Jul. 2006.
- [32] C. S. Park and K. B. Lee, "Transmit power allocation for BER performance improvement in multicarrier systems," *IEEE Trans. Commun.*, vol. 52, no. 10, pp. 1658–1663, Oct. 2004.
- [33] A. F. Molisch et al., "IEEE 802.15.4a channel model—Final report," IEEE 802.15 WPAN Low Rate Alternative PHY Task Group, Tech. Rep., Nov. 2004.
- [34] A. A. M. Saleh and R. Valenzuela, "A statistical model for indoor multipath propagation," *IEEE J. Sel. Areas Commun.*, vol. JSAC-5, no. 2, pp. 128–137, Feb. 1987.
- [35] *Wireless LAN Medium Access Control (MAC) and Physical Layer (PHY) Specifications*, IEEE Standard 802.11ax, 2021.
- [36] T. S. Rappaport, *Wireless Communications: Principles and Practice*, 2nd ed., Upper Saddle River, NJ, USA: Prentice-Hall, 2001.
- [37] N. Cravo, M. de L. Filomeno, and M. V. Ribeiro, "Hybrid power line/wireless systems: Analyses of normalized SNRs for in-home broadband scenarios," in *Proc. 40th Simpósio Brasileiro de Telecomunicações e Processamento de Sinais*, Santa Rita do Sapucaí, Brazil, Sep. 2022, pp. 1–5.
- [38] T. F. Moreira, Â. Camponogara, S. Baig, and M. V. Ribeiro, "Performance analysis of orthogonal multiplexing techniques for PLC systems with low cyclic prefix length and symbol timing offset," *Sensors*, vol. 23, no. 9, p. 4363, Apr. 2023.
- [39] H. Cheon and D. Hong, "Effect of channel estimation error in OFDM-based WLAN," *IEEE Commun. Lett.*, vol. 6, no. 5, pp. 190–192, May 2002.
- [40] L. Rugini and P. Banelli, "BER of OFDM systems impaired by carrier frequency offset in multipath fading channels," *IEEE Trans. Wireless Commun.*, vol. 4, no. 5, pp. 2279–2288, Sep. 2005.
- [41] A. Viterbi, "Convolutional codes and their performance in communication systems," *IEEE Trans. Commun. Technol.*, vol. CT-19, no. 5, pp. 751–772, Oct. 1971.
- [42] J. Hou, P. H. Siegel, L. B. Milstein, and H. D. Pfister, "Capacity-approaching bandwidth-efficient coded modulation schemes based on low-density parity-check codes," *IEEE Trans. Inf. Theory*, vol. 49, no. 9, pp. 2141–2155, Sep. 2003.
- [43] S. H. Han and J. H. Lee, "An overview of peak-to-average power ratio reduction techniques for multicarrier transmission," *IEEE Wireless Commun.*, vol. 12, no. 2, pp. 56–65, Apr. 2005.
- [44] J. L. G. Monsalve, "Green OFDM a new method for OFDM PAPR reduction," Ph.D. dissertation, Dept. Automatique et Traitement du Signal, Communauté Université Grenoble Alpes, Saint-Martin-d'Hères, France, 2019.



Túlio Fernandes Moreira received the B.Sc. and M.Sc. degrees in electrical engineering from the Federal University of Juiz de Fora (UFJF), Brazil, in 2020 and 2022, respectively. He is currently pursuing the D.Sc. degree in electrical engineering, during which he was granted a six-month PDSE-CAPES Scholarship to conduct research as a Visiting Scholar at the Institut Supérieur de l'Aéronautique et de l'Espace (ISAE-SUPAERO), Université de Toulouse, France. His research interests include digital signal processing and communication, with a particular focus on multicarrier modulation techniques for power line, wireless, and satellite communication systems.



Mateus de Lima Filomeno received the B.S. degree in electrical engineering with a major in telecommunications and the M.Sc. and D.Sc. degrees in electrical engineering in the area of electronic systems from the Federal University of Juiz de Fora (UFJF), Brazil, in 2016, 2018, and 2022, respectively.

In 2023, he received the Honorable Mention in the Brazilian D.Sc. Dissertation Award from Capes, Brazil, in the Engineering IV category, which encompasses electrical and biomedical engineering.

He currently works as a Post-Doctoral Researcher with UFJF. His research interests include signal processing, digital communication, information theory, power line communication, wireless communication, and hybrid communication.



Wallace Alves Martins (Senior Member, IEEE) received the Electronics Engineer degree and the M.Sc. and D.Sc. degrees in electrical engineering from the Federal University of Rio de Janeiro (UFRJ), Rio de Janeiro, Brazil, in 2007, 2009, and 2011, respectively. From 2019 to 2023, he worked as a Researcher with the Interdisciplinary Centre for Security, Reliability, and Trust (SnT), University of Luxembourg. He was affiliated with UFRJ from 2013 to 2022, working as an Associate Professor. During this period, he also held roles

as an Academic Coordinator of the electronics and computer engineering undergraduate course and the Deputy Department Chairman (DEL/Poli/UFRJ) from 2016 to 2017. He was also a Research Visitor with the University of Notre Dame, USA, in 2008, Université de Lille 1, France, in 2016, and Universidad de Alcalá, Spain, in 2018. He is currently a Full Professor with the Institut Supérieur de l'Aéronautique et de l'Espace (ISAE-SUPAERO), Université de Toulouse, France. His research interests include digital signal processing and telecommunications, with a focus on future satellite networks. He was a recipient of the Best Student Paper Award from EURASIP at EUSIPCO-2009, Glasgow, Scotland, the 2012 Best Brazilian D.Sc. Dissertation Award from Capes, Brazil, and the Best Paper Award at SBrT-2020, Florianópolis, Brazil. He currently serves as a Senior Area Editor for IEEE SIGNAL PROCESSING LETTERS, an Editor for IEEE COMMUNICATIONS LETTERS, and an Associate Editor for *EURASIP Journal on Advances in Signal Processing*. He also serves on the EURASIP Technical Area Committee (TAC) Theoretical and Methodological Trends in Signal Processing (TMTSP).



Moisés Vidal Ribeiro (Senior Member, IEEE) received the B.S. degree in electrical engineering from the Federal University of Juiz de Fora (UFJF), Brazil, in 1999, and the M.Sc. and D.Sc. degrees in electrical engineering from the University of Campinas, Brazil, in 2001 and 2005, respectively.

He was a Visiting Scholar with the University of California at Santa Barbara, CA, USA, in 2004, a Visiting Professor from 2005 to 2007, and an Assistant Professor with UFJF from 2007 to 2015, where he has been a Full Professor since 2015. He is

currently the Director of the Brazilian National Institute of Science and Technology for Electricity (INERGE). He co-founded Smart9 Ltd., and Wari Ltd., in 2012 and 2015, respectively. He has served as the Secretary for the IEEE ComSoc TC-PLC. He has advised 46 graduate students in these fields and authored over 256 peer-reviewed articles and nine book chapters. He holds 13 issued/pending patents. His research interests include signal processing, power line communication, wireless communication, artificial intelligence, and satellite communication.

Dr. Ribeiro was a recipient of the Fulbright Visiting Professorship at Stanford University, Stanford, CA, USA, in 2011, and Princeton University, Princeton, NJ, USA, in 2012. He was the General Chair of the 2010 IEEE ISPLC, 2013 IWSSC, SBrT 2015, and 2023 SIoT, and a Guest Co-Editor of Special Issues of the *EURASIP Journal on Advances in Signal Processing* and *EURASIP Journal of Electrical and Computer Engineering*. He was awarded Student Awards from 2001 IEEE IECON and 2003 IEEE ISIE, a winner of the 2014 I2P Global Competition, the Honorable Mention in 2014 Global Venture Labs Investment Competition, the Third Place Prêmio Mineiro de Inovação in 2014, the Engie Brazil Innovation Award in 2016, Unicamp Inventor Awards in 2017 and 2018, and the 2021 TC-PLC Outstanding Service Award from the IEEE ComSoc TC-PLC.